Granular Matter (2019) 21:105
https://doi.org/10.1007/s10035-019-0961-z

ORIGINAL PAPER

Influence of particle size on vertical plate penetration into dense cohesionless granular materials (large-scale DEM simulation using real particle size)

Shinichiro Miyai[1,2,3] · Murino Kobayakawa[3] · Takuya Tsuji[1,3] · Toshitsugu Tanaka[1,3]

Received: 16 April 2019 / Published online: 13 October 2019
© The Author(s) 2019

Abstract
The influence of the particle size on the vertical plate penetration into dense cohesionless granular materials was numerically investigated. Simulations were performed in quasi-two-dimensional conditions by changing the mean particle diameters d_{50} but maintaining the plate thickness B from $B/d_{50}=63$–2.6. The initial bulk packing fraction was kept high, irrespective of the particle size. In the smallest particle size case ($B/d_{50}=63$), the size ratio reached almost the same level as that in the laboratory experiments using natural sand particles. The results demonstrated that the mean penetration resistance force acting on the plate tip surface increases with a decrease of B/d_{50}, while the tangential force acting on the side surfaces does not change with B/d_{50}. Tip resistances increase linearly with the penetration depth, while the tangential resistances increase with the square of the depth regardless of B/d_{50}. The behavior of the resistance fluctuations changes qualitatively between $B/d_{50}=31$ and 21. For all cases, we confirmed the formation of a wedge-shaped flow with a high forward velocity in front of the plate tip. The wedge flow width was larger than the plate thickness by almost a mean particle diameter, and was responsible for the increase in the mean resistance depending on the particle size. For the large B/d_{50} cases only, the resistance exhibited quasi-periodic fluctuations, which was attributable to the intermittent nucleation and disappearance of the shear bands. Moreover, we investigated the dependence of B/d_{50} on the band evolutions by analyzing the band thickness.

Keywords Penetration · Resistance force · Shear band · Cohesionless granular materials · Discrete element method (DEM)

1 Introduction

The resistance force acting on intruders during penetration into granular materials is of interest not only in granular physics [1–12], but also in engineering applications, such as cone penetration tests [13–21], pile installations [22–28], the digging of mining machineries [29], and the locomotion of legged robots over rough terrain [30]. Previous studies have demonstrated that the penetration resistance is affected by the particle size [12, 14, 16, 17, 20, 21, 31], bulk packing fraction [2, 9, 12, 17, 19, 21, 25], penetration depth [3, 4, 7, 8, 12, 24, 25], intruder shape [3, 4, 20, 27, 29], and penetration velocity [9, 18]. Despite numerous efforts in these previous studies, the understanding of the underlying mechanisms of penetration resistance remains insufficient, owing to the inherent complexity of the particle–object interactions.

In this study, we focused on the influence of the particle size on the penetration resistance and behavior of granular materials. Bolton et al. [14] experimentally demonstrated that the penetration resistance acting on a cone penetrometer is influenced by the particle size. These authors used sand particles with different median diameters ($d_{50}=0.225$, 0.40, and 0.90 mm). These sand particles had almost the same mechanical properties, with different particle size distributions and bulk packing fractions. By means of penetration tests with varying cone diameters B from 6.35 to 19.05 mm, they evaluated the relative particle size effect.

Electronic supplementary material The online version of this article (https://doi.org/10.1007/s10035-019-0961-z) contains supplementary material, which is available to authorized users.

✉ Takuya Tsuji
tak@mech.eng.osaka-u.ac.jp

1 Department of Mechanical Engineering, Osaka University, Suita, Osaka, Japan

2 Development Division, Komatsu Ltd, Hiratsuka, Kanagawa, Japan

3 Komatsu MIRAI Construction Equipment Cooperative Research Center, Osaka University, Suita, Osaka, Japan

For cases of fine sand particles with B/d_{50} ranging from 28 to 85, the resistances were not affected. However, for medium and coarse sand particle cases using the smallest cone ($B/d_{50}=16$ and 7, respectively), the resistances increased. They suggested that cone penetration tests should be performed using cones with diameters 20 times larger than the particle diameter to diminish the dependence on B/d_{50}, but the detailed mechanism of this dependence was not clarified in their study. Experiments by Peng et al. [3] and Kang et al. [7] also demonstrated that the influence of the particle size on the penetration resistance was negligibly small in the regime ($B/d_{50}>20$). Cerato and Lutenegger [32] suggested that the size effect was closely related to mesoscopic structure evolutions, such as the formation of shear bands. They speculated that shear bands induced by penetrations could not propagate fully with a decreasing B/d_{50}. However, they did not observe shear band formations in their study, and their theories have not been confirmed. Hamm et al. [1] and Tapia et al. [2] observed plate penetrations using an image analysis technique under sufficiently larger B/d_{50} conditions ($B/d_{50}\approx 60$). They demonstrated that shear band formation could be observed at a dense initial bulk packing fraction ($\varphi_0>0.6$). Moreover, they found that, for the dense case, the shear band evolutions were strongly related to the penetration resistance response. These results indicated that mesoscopic structural evolutions play an important role in object penetrations. However, the mechanism of the particle size effects on the penetration resistance and its influence on granular behaviors are still not effectively understood, as it is inherently difficult to change the particle size solely and observe the dynamics of mesoscopic structures and individual particles in experiments.

In recent years, numerical simulations based on the discrete element method (DEM) have been extensively employed to investigate the micro–macro behaviors of granular materials. The DEM is capable of changing the particle-scale properties as intended. However, in general, there exists a limitation on the total number of particles for obtaining DEM simulation results within a reasonable computation time. Numerous researchers have reduced the total number of particles by increasing the particle size. It is apparent that this approach is not adequate for investigating the particle size effect. As indicated in Table 1, DEM studies have been limited to small B/d_{50} conditions excepting our previous study [31], and the shear band formation in granular materials has not been clearly observed during object penetration. In our previous study [33], a DEM program code was parallelized based on the dynamic domain decomposition technique, and could handle tens of millions of particles. To investigate the particle size effect, we conducted large-scale DEM simulations of vertical plate penetration into dense cohesionless granular materials in quasi-two-dimensional conditions using 67.9 million particles for the maximum case ($d_{50}=0.233$ mm) [31]. In the simulations, by varying the mean particle size but maintaining the plate width ($B=20$ mm), we changed B/d_{50} from 1.3 to 86. The results demonstrated that the penetration resistance increases with a decreasing B/d_{50}, and were consistent with the findings of Bolton's cone penetration tests [14]. We demonstrated that for small particles only ($B/d_{50}=86$), discontinuous shear band evolution could be clearly observed in the bed, and penetration resistance appeared with quasi-periodicity. The results exhibited qualitative agreements with the experimental studies by Hamm et al. [1] and Tapia et al. [2]. In contrast, for small B/d_{50} cases, discontinuous shear band formation could not be clearly confirmed. In the paper, however, a value of B/d_{50} where the change occurs was not clarified. Moreover, the mechanisms that B/d_{50} affects penetration resistance and shear band formation have not been revealed.

In this study, we investigated the B/d_{50} dependence of the penetration resistance and shear band formation in a dense granular material by changing B/d_{50} extensively and maintaining the other conditions, such as the particle shape and initial bulk packing fraction. Firstly, we confirmed the validity of the DEM plate penetration model employed in this study by means of comparisons with the experimental results. Secondly, we performed numerical penetration tests by changing B/d_{50} from 63 to 2.6 in quasi-two-dimensional conditions. For $B/d_{50}=63$, the ratio was equivalent to that in the experiments by Hamm et al. [1] and Tapia et al. [2], which was a considerably large-scale DEM simulation with a maximum of 35.5 million particles used. Thereafter, we illustrated the B/d_{50} dependence of the penetration resistance

Table 1 Review of studies on B/d_{50} dependence of penetration resistance

References	Method	Intruder	The number of particles	B/d_{50}
Bolton et al. [14]	Experiment	Cone penetrometer	–	7–85
Previous study [31]	DEM simulation (3D)	Flat plate (Quasi-2D)	67,928,040 ($B/d_{50}=86$)	1.3, 11, 86
Feng et al. [12]	DEM simulation (3D)	Cylinder	2,940,000 ($B/d_{50}=30$)	15, 21, 30
Butlanska et al. [16]	DEM simulation (3D)	Cone penetrometer	65,000	2.7, 4, 5.4, 8
Liu and Wu [20]	DEM simulation (3D)	Cone penetrometer	422,191	3, 6, 12
Liu and Wang [21]	DEM simulation (2D)	Cone penetrometer	695,649 ($B/d_{50}=18$)	9, 18

and explored a value of B/d_{50} at which the tendencies of the resistance and granular behaviors changed. Finally, we analyzed the granular flow and shear band formation at the particle scale and discussed the mechanisms whereby B/d_{50} affects the penetration resistance and shear band formation.

2 Methodology

2.1 DEM

In the DEM, the dynamics of granular materials were obtained by solving the equations of motion for individual particles. The contact forces were modeled by combinations of a linear spring, dashpot, and frictional slider [34]. Although the use of commercially available glass beads with high sphericity was assumed in this study, real glass beads will always have a certain degree of non-sphericity. A rolling resistance model that suppresses the excessive relative rotation of contacting particles owing to the non-sphericity was also introduced. Several rolling resistance models have been proposed [35–37], and the rolling spring-dashpot-slider model presented by Jiang et al. [38] was employed in this study. This model has two components in the rolling and twisting directions, respectively. As illustrated in Fig. 1, the rolling axis is defined on the contact plane, which is perpendicular to the vector from the center of particle i to the center of particle j, while the twisting axis is defined in the direction perpendicular to the contact plane. The translational and rotational motion equations of particle i are respectively expressed by

$$m_i \frac{d\boldsymbol{v}_i}{dt} = \sum_j \left(\boldsymbol{F}_N^j + \boldsymbol{F}_S^j \right) + m_i \boldsymbol{g} \tag{1}$$

$$I_i \frac{d\boldsymbol{\omega}_i}{dt} = \sum_j \left(\boldsymbol{r}_i^j \times \boldsymbol{F}_S^j + \boldsymbol{M}_R^j + \boldsymbol{M}_T^j \right), \tag{2}$$

where m_i, I_i, $\boldsymbol{v}_i$, and $\boldsymbol{\omega}_i$ are the mass, moment of inertia, velocity, and angular velocity of particle i, respectively; $\boldsymbol{F}^j{}_N$ and $\boldsymbol{F}^j{}_S$ are the normal and tangential forces acting on particle i by contacting particle j, respectively; $\boldsymbol{r}^j{}_i$ is the vector from the center of particle i to the contact point with particle j; $\boldsymbol{M}^j{}_R$ is the rolling moment; $\boldsymbol{M}^j{}_T$ is the twisting moment owing to the rolling resistance; and $\boldsymbol{g}$ is the gravity acceleration. Frictional sliders were provided in the tangential, rolling, and twisting directions, which limited the forces and moments to certain values, as illustrated in Fig. 2. The tangential force, and the rolling and twisting resistive moments, respectively, are described as follows:

$$\boldsymbol{F}_N^j = \left(k_N \delta_N + c_N v_N \right) \frac{\boldsymbol{v}_N}{|\boldsymbol{v}_N|} \tag{3}$$

$$\boldsymbol{F}_S^j = \min\left(k_S \delta_S + c_S v_S, \mu \left| \boldsymbol{F}_N^j \right| \right) \frac{\boldsymbol{v}_S}{|\boldsymbol{v}_S|} \tag{4}$$

$$\boldsymbol{M}_R^j = \min\left(k_R \theta_R + c_R \omega_R, 0.25 \zeta_C \beta r \left| \boldsymbol{F}_N^j \right| \right) \frac{\boldsymbol{\omega}_R}{|\boldsymbol{\omega}_R|} \tag{5}$$

$$\boldsymbol{M}_T^j = \min\left(k_T \theta_T + c_T \omega_T, 0.65 \mu \beta r \left| \boldsymbol{F}_N^j \right| \right) \frac{\boldsymbol{\omega}_T}{|\boldsymbol{\omega}_T|}, \tag{6}$$

where k and c are the spring constant and viscous damping, respectively, while the suffixes N, S, R, and T represent the normal, tangential, rolling, and twisting directions,

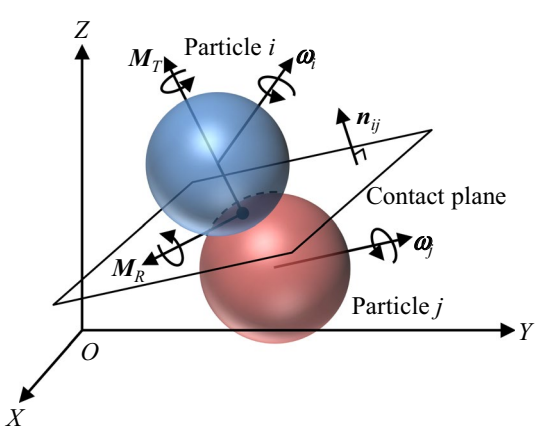

Fig. 1 Rolling and twisting moments of contact between particles

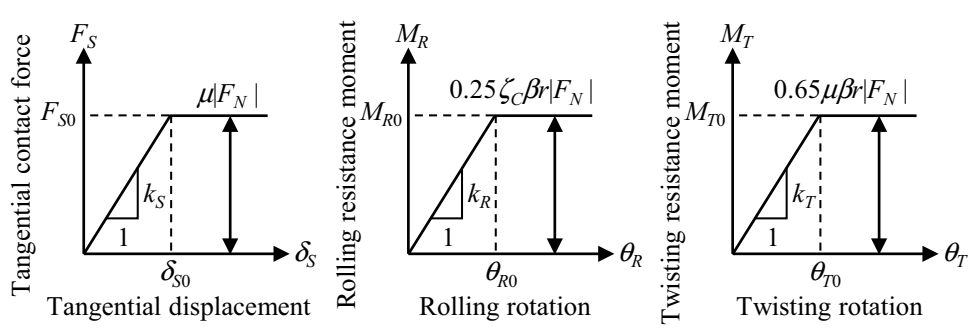

Fig. 2 Tangential, rolling and twisting contact response system

respectively. Moreover, δ_N and δ_S is the normal and tangential displacements, while θ_R and θ_T are the rolling and twisting rotations; $\boldsymbol{v}_N$, $\boldsymbol{v}_S$, $\boldsymbol{\omega}_R$, and $\boldsymbol{\omega}_T$ are the relative normal, tangential velocity, rolling angular velocity, and twisting angular velocity, respectively; $\boldsymbol{\omega}_R$ and $\boldsymbol{\omega}_T$ are calculated as $\boldsymbol{\omega}_R+\boldsymbol{\omega}_T=\boldsymbol{\omega}_i-\boldsymbol{\omega}_j$ and $\boldsymbol{\omega}_T=[(\boldsymbol{\omega}_i-\boldsymbol{\omega}_j)\cdot\boldsymbol{n}_{ij}]\boldsymbol{n}_{ij}$, respectively, where $\boldsymbol{n}_{ij}$ is the unit vector from particle j to particle i; r is the common radius of the particles, defined as $r=2r_ir_j/(r_i+r_j)$; μ is the coefficient of sliding friction; and β and ζ_C are the rolling resistance model parameters. Jiang et al. [38] described the particle shape effect according to the dimensionless shape parameter β. For a perfect spherical particle, β is set to 0. The local resistance owing to asperity crushing is described by the dimensionless local crushing parameter ζ_C. Furthermore, they proposed a simplified model in which ζ_C is equal to 2.1.

2.2 Calculation conditions

2.2.1 DEM parameter setup

The properties of the glass beads used in this study are shown in Table 2. Glass beads #1 and #2 had different median diameters, while the other properties such as the shape and density were similar. For all of the plate penetration tests discussed in the following section, the properties of glass beads #1 ($d_{50}=0.32$ mm), such as the particle size distribution, particle density ρ, coefficient of sliding friction μ (the coefficients of the particle–particle, particle–acrylic wall, and particle–stainless plate frictions were 0.31, 0.20, and 0.27, respectively), and the coefficient of restitution e (0.9) were used. Glass beads #2 were used to obtain the shape parameter β and validate our DEM model. Figure 3 illustrates the size distributions of the glass beads and DEM particles. In the DEM simulations, different particle diameter sets of $d=0.31$, 0.32, 0.33, and 0.34 mm and $d=1.8$, 1.9, and 2.0 mm were respectively used so as the median diameter d_{50} and uniformity coefficient d_{60}/d_{10} are equivalent to glass beads #1 and #2. In the linear spring model, the spring constant cannot be directly related to the material properties of the particles. The normal spring constant k_N was determined such that the particle stress based on the amount of overlap in the normal direction becomes equivalent regardless of d_{50} [39, 40]. When the spring constant

Table 2 Properties of glass beads #1 and #2

Glass beads	Median diameter d_{50} (mm)	Uniformity coefficient d_{60}/d_{10}	Particle density ρ (kg/m^3)
#1	0.32	1.1	2610
#2	1.86	1.1	2490

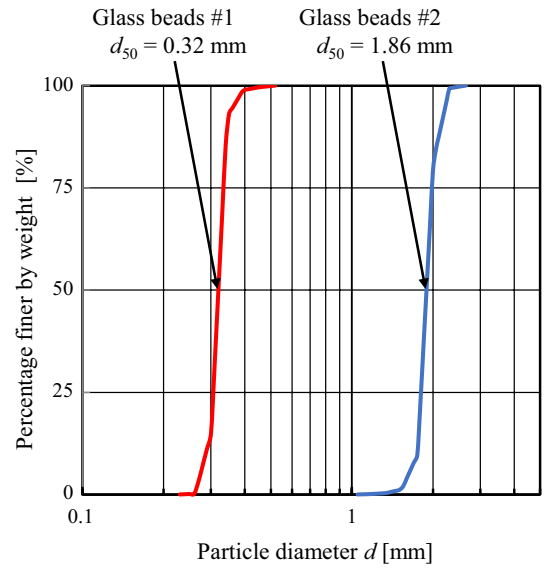

Fig. 3 Size distributions of glass beads #1 (red line) and #2 (blue line). Uniformity coefficients d_{60}/d_{10} were 1.1 for both types of beads. In the calibration and validation tests, the distributions for the DEM model were given based on glass beads #2. After Sect. 2.2.3, the distributions for the DEM model were determined based on glass beads #1 (color figure online)

becomes excessively small, the amount of particle overlaps becomes large, and the overall behaviors of the granular materials may be altered [41]. For glass beads #2, the normal spring constant k_N was chosen as 8.3×10^4 N/m according to preliminary computations in which k_N was varied within the range from 6.0×10^3 to 1.6×10^6 N/m. This value was used because the values in the range from 8.3×10^4 to 1.6×10^6 N/m did not substantially affect the penetration force working on the plate. Furthermore, in the case $k_N\geq8.3\times10^4$ N/m, particle overlaps in the normal direction were always less than 1% of the particle diameters. The normal viscous damping c_N was determined from the coefficient of restitution of the particles [42]:

$$c_N=-\frac{2\ln e}{\sqrt{\pi^2+(\ln e)^2}}\sqrt{m_ik_N}. \tag{7}$$

The tangential spring constant k_S and viscous damping c_S were calculated by $\nu=k_S/k_N$ and $\nu^2=c_S/c_N$, respectively, where ν is the Poisson's ratio of glass (0.25). The rolling spring constant k_R, twisting spring constant k_T, rolling viscous damping c_R, and twisting viscous damping c_T were calculated by $k_R=0.25(\beta r)^2\,k_N$, $k_T=0.5(\beta r)^2\,k_S$, $c_R=0.25(\beta r)^2\,c_N$, and $c_T=0.5(\beta r)^2\,c_S$, respectively [38]. The shape parameter β was calibrated by the comparison between the experimental and numerical results of the cone penetration tests, because it is not trivial to measure the parameter.

The calibration study was conducted using glass beads #2 (d_{50} = 1.86 mm). A stainless cone was penetrated vertically into the cohesionless granular materials with a constant speed of 10 mm/s in a rectangular container with a 218 mm width, 210 mm depth, and 150 mm height. As illustrated in Fig. 4, the cone was equipped with a tip of 30° and base of 28.6 mm in diameter. The cone penetration calculations were performed by varying the shape parameter β. When β = 0.04, the cone penetration force exhibited good agreements with the experimental results, as indicated in Fig. 4.

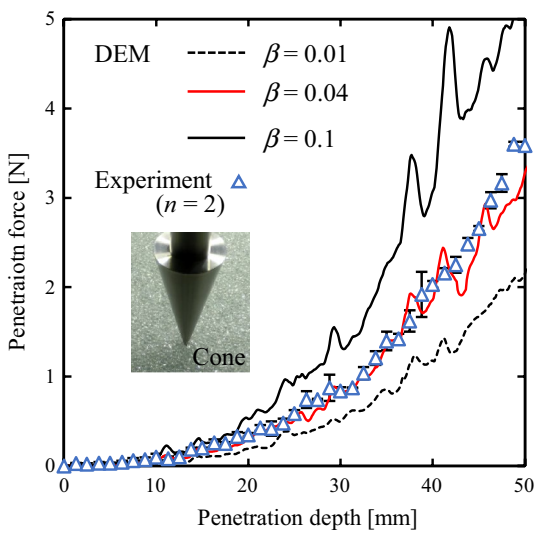

Fig. 4 Comparison of penetration force in simulation (lines) and experiment (triangles) in calibration tests for shape factor β. Triangles and their error bars represent the means and standard deviations of the two experimental trials, respectively

2.2.2 Validation testing of the DEM model

To validate the presented DEM model, we also performed plate penetration tests experimentally, and the results were compared. As illustrated in Fig. 5, glass beads #2 were randomly packed in a rectangular container with a 1000 mm width (W), 100 mm depth (D), and 400 mm height. The initial bulk packing fraction φ_0 was set to $\varphi_0 \approx 0.63$ by tapping the container. The initial bed height was set to 300 mm. The container side walls were made of acrylic to enable visual observations during penetration. A stainless flat plate with a 96 mm depth, 20 mm (B) thickness, and 250 mm height was used in the experiments. The plate had a similar surface roughness to the cone used in the parameter calibrations. The plate was penetrated vertically into the bed at a constant speed of V_P = 100 mm/s until the front tip reached a depth of 150 mm from the initial bed surface. We confirmed that the penetration resistance does not depend on the penetration speed in this regime. Further discussions will be developed in Sect. 3.1. During the penetrations, the penetration force F_z acting on the plate was measured by a load cell attached to the plate base. The container width was sufficiently large relative to the plate thickness, and the influence of the sidewalls at both ends was negligible. The parameters used in the DEM calculations are displayed in Table 3. The particles with d = 1.8, 1.9, and 2.0 mm were used such that the number ratio became 3:4:3. The initial random bed was obtained by falling particles with random initial velocities under gravity. The initial bulk packing fraction φ_0 was controlled by varying the coefficient of sliding friction and shape factor during the packing process; φ_0 was set to 0.63, corresponding to the experiments. Following packing, the coefficient of sliding friction and the shape factor were set to the predetermined values displayed in Table 3. After the change of coefficients, the beds were relaxed until they reached a

Fig. 5 Plate penetration conditions for the validation test of the DEM model

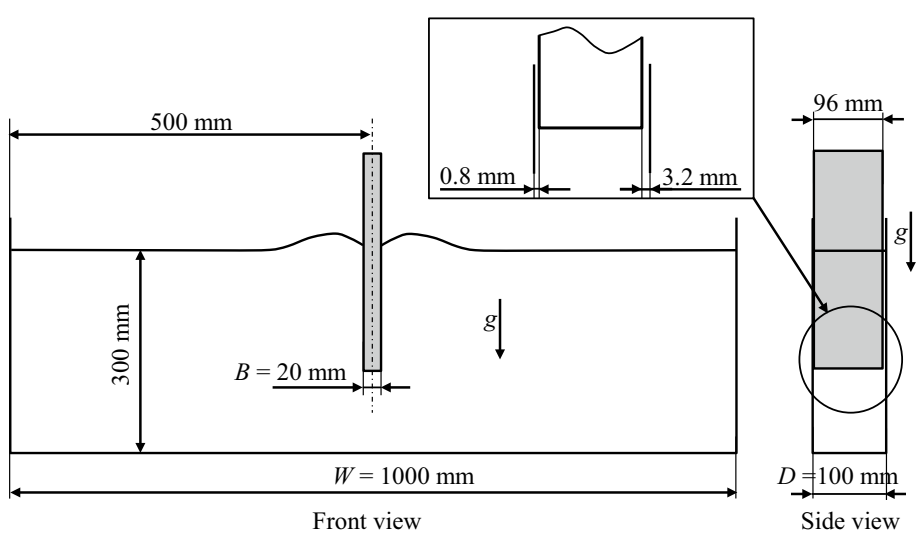

Table 3 DEM parameters for glass beads #2 for validation test

Parameter	Unit	Value
Particle diameter d	(mm)	1.8, 1.9, 2.0
Normal spring constant k_N	(N/m)	8.3×10^4
Coefficient of restitution e	(–)	0.9
Poisson's ratio ν	(–)	0.25
Particle density ρ	(kg/m^3)	2490
Coefficient of sliding friction μ		
Particle–particle	(–)	0.31
Particle–wall	(–)	0.20
Particle–plate	(–)	0.27
Shape parameter β	(–)	0.04
Local crushing parameter ζ_C	(–)	2.1

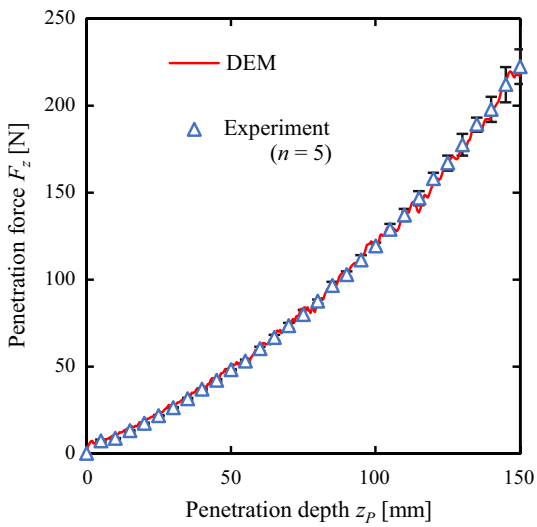

Fig. 6 Comparison of penetration forces in simulation (red line) and experiment (triangles) in the validation test for the DEM model. Triangles and their error bars represent the means and standard deviations of the five experimental trials, respectively (color figure online)

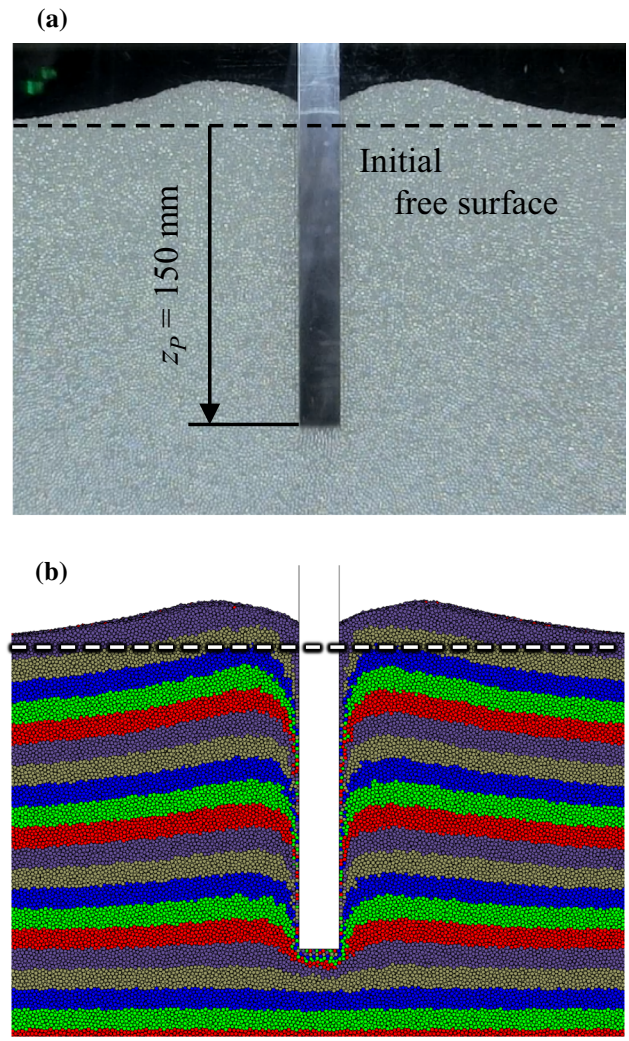

Fig. 7 Comparison of granular bed behaviors in **a** experiment and **b** simulation in the validation test for the DEM model, showing snapshots at the penetration depth $z_P = 150$ mm. Dashed lines indicate the initial free surfaces of the bed

steady state. We confirmed that the packing fraction of the beds was the same before and after the relaxation.

Figure 6 illustrates the penetration resistance force, while Fig. 7 illustrates the particle bed deformation when the plate reached a depth of 150 mm. The particles are colored according to their initial vertical positions (10 mm intervals) to make the deformations visible. Good agreements were observed between the presented DEM and experiment for both the force and bed deformation.

2.2.3 Plate penetration model setup

As illustrated in Fig. 8, all simulations were performed in quasi-two-dimensional computational domains, in which the periodic boundary condition was used in the depth (x) direction. A flat plate assuming periodicity in the x direction was pushed vertically into the cohesionless granular beds with a constant speed of $V_P = 100$ mm/s. Cases A–F were compared, with different mean particle diameters, as listed in Table 4. For all cases, the plate thickness B was set to 20 mm. Hence, the ratio of the plate thickness to the median particle diameter B/d_{50} was changed from 2.6 to 63. The smallest particles were used in Case A ($d_{50} = 0.32$ mm), where the relative particle size ($B/d_{50} = 63$) reached almost the same level as that in previous laboratory experiments [1, 2]. This was a considerably large-scale DEM simulation, because the total number of particles in the bed was 35.5 million (Case A: $d_{50} = 0.32$ mm).

The computational domain size in the periodic direction was at least 20 times larger than the maximum particle diameter in each case. The computational domain width

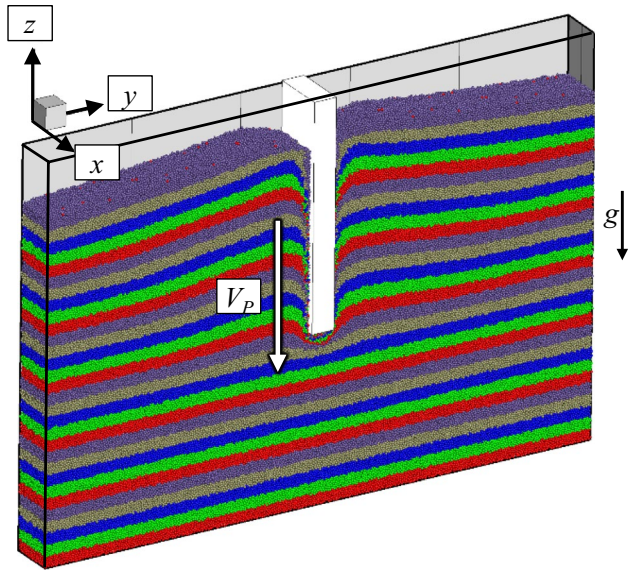

Fig. 8 Plate penetration DEM simulation in quasi-two-dimensional computational domain. Periodic boundary conditions are used in the depth (x) direction

W in the y direction was set to be large as the domain size effect became negligible. To examine the influence of the domain size effect and boundary conditions on the penetration force, we performed simulations using different conditions, and the results are presented in Fig. 9. With the exception of the domain width W in the y direction and boundary conditions in the x direction, the other calculation parameters were the same as in the validation simulation in the former section. We found that in the case of $W = 500$ mm, the penetration force was almost the same as in the case of $W = 1000$ mm, until the penetration depth reached 150 mm. This result indicates that the value was sufficient to prevent the domain size effect if $W \geq 500$ mm. Thus, for the cases from $d_{50} = 0.32$–3.84 mm (Case A–E), W was set to 500 mm, while for $d_{50} = 7.68$ mm (Case F), W was set to 1000 mm. In terms of the boundary conditions, the penetration forces in the frictional and frictionless fixed-wall boundary condition were larger than that in the periodic boundary condition because the fixed-walls prevent particle motion in the x direction.

The particle size distribution and particle density in DEM calculations were determined according to the glass beads #1 in Fig. 3 and Table 2. For Case A, particles with $d = 0.31$, 0.32, 0.33 and 0.34 mm were randomly packed such that the number ratio became 1:2:2:1. For Cases B–F, the relative particle size relation was kept but it was adjusted to realize the targeted median diameter d_{50}. For example, $d = 0.62$, 0.64, 0.66, and 0.68 mm were adopted for Case B. The particle density ρ was set to 2610 kg/m^3. For all particle size cases, the initial packing fraction φ_0 of the beds was set to 0.63. Simulations were performed until the penetration depth z_p, which is the distance from the plate front tip to the initial bed free surface, reached 150 mm. All calculations were performed in three dimensions.

3 Results

3.1 Penetration resistance

The penetration resistance force F_z can be decomposed into the normal force working on the front surface F_{Tip}, and the tangential forces on the left surface F_{Left} and right surface F_{Right}. Figure 10 illustrates the penetration depth dependence of F_{Tip} and the sum of F_{Left} and F_{Right}. The vertical axis represents the penetration resistance, while the horizontal axis represents the penetration depth z_P. To enable comparisons, the penetration resistances were normalized by S_P (depth of periodic domain $D \times$ plate thickness B). In Fig. 10a, the results of penetration speed $V_p = 50$ mm/s are also shown for Case A ($B/d_{50} = 63$). It was confirmed that the resistances including fluctuations are not sensitive to the penetration speed in this regime. For all cases, both F_{Tip} and the sum of F_{Left} and F_{Right} increased with the penetration depth and F_{Tip} is the major contribution to the penetration resistance. Figure 11 shows the transitions of F_{Tip} with respect to penetration depth

Table 4 Summary of quasi-two-dimensional penetration tests using DEM

Case	Particle size d (mm)	Median diameter d_{50} (mm)	B/d_{50} (–)	Dimensions of granular bed D (x) × W (y) × H (z) (mm)	Initial packing fraction φ_0 (–)	Normal spring constant k_N (N/m)
A	0.31–0.34	0.32	63	6.8 × 500 × 300	0.63	1.6×10^4
B	0.62–0.68	0.64	31	13.6 × 500 × 300	0.63	3.2×10^4
C	0.93–1.02	0.96	21	20.4 × 500 × 300	0.63	4.8×10^4
D	1.86–2.04	1.92	10	40.8 × 500 × 300	0.63	9.6×10^4
E	3.72–4.08	3.84	5.2	81.6 × 500 × 300	0.63	1.92×10^5
F	7.44–8.16	7.68	2.6	163.2 × 1000 × 300	0.63	3.84×10^5

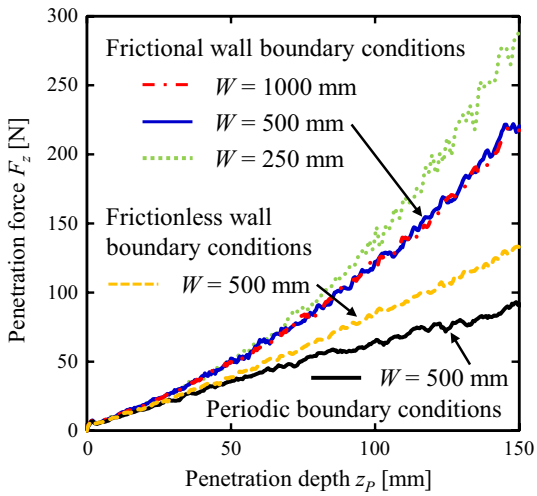

Fig. 9 Influence of boundary conditions in the x direction and domain width W in the y direction on penetration forces using DEM. The green dotted line, blue solid line, and red dashed line represent the cases of domain width W of 250, 500, and 1000 mm, respectively. The yellow dashed line and black solid line represent cases of frictionless wall and periodic boundary conditions with $W = 500$ mm (color figure online)

using $F_{Tip}/(S_P \times z_P)$. F_{Tip} increased immediately after the penetration started and increased almost linearly with the penetration depth after $z_P \approx 20$ mm. Hereafter, we refer to the depth with $z_P \geq 20$ mm as the *linear regime*. In Fig. 10, linear fitting lines $p(z_P)$ for F_{Tip}/S_P of $z_P \geq 20$ mm are also plotted. F_{Tip} is a hydrostatic-like force that depends on the penetration depth. Figure 12 shows the depth dependence of F_{Left} and F_{Right} of all the cases. The sum of F_{Left} and F_{Right} increased super-linearly with the penetration depth irrespective of B/d_{50}. It is expected that friction between particles and plates is the major contribution to the tangential forces working on the side surfaces and can be given by

$$F_{Left}, F_{Right} = \mu_{particle-plate} D \int_0^{z_B} P_y(z) dz, \tag{8}$$

where $P_y(z)$ is the earth pressure working normal to the side surfaces of the plate, $\mu_{particle-plate}$ is the coefficient of friction between particles and the plate, and z_B is the depth from the free surface of the bed to the plate tip. Assuming that the earth pressure increases linearly with depth $P_y(z) \sim z$ and z_B is equal to z_P, F_{Left} and F_{Right} are proportional to the square of z_P; F_{Left} and $F_{Right} \sim z_P^2$. A fitting curve $q(z_P)$ as a function of the square of penetration depth follows the data quite closely, as shown in Fig. 12. Superposing the linearity of the normal force working on the front surface and the non-linearity of tangential forces on the side surfaces, a total force F_z shows a slight non-linearity as demonstrated in Fig. 10d.

To investigate the influence of the particle size, F_{Tip}/S_P and the linear fitting lines $p(z_P)$ for all the cases are plotted in Fig. 13. Clearly, as B/d_{50} decreased, the mean tip penetration resistance increased, which is consistent with the experiments by Bolton et al. [14]. In Fig. 14, fluctuations in F_{Tip} can be observed for all the cases. Figure 14 illustrates the resistance fluctuations $\Delta P = F_{Tip}/S_P - p(z_P)$ for Case A ($B/d_{50} = 63$), Case B ($B/d_{50} = 31$), Case C ($B/d_{50} = 21$), and Case D ($B/d_{50} = 10$). The fluctuations became quasi-periodic when $B/d_{50} \geq 31$. For $B/d_{50} = 63$, ΔP exhibited a quasi-periodic cycle at almost 20 mm intervals along with the plate advancement. For $B/d_{50} = 31$, ΔP exhibited a quasi-periodic cycle at almost 25 mm, until z_P reached almost 100 mm. The quasi-periodic fluctuations in the resistance were similar to the results reported by Hamm et al. [1] and Tapia et al. [2]. Meanwhile, for $B/d_{50} = 21$ and 10, ΔP did not exhibit a clear trend. We found that the tendency of the resistance fluctuations changed between $B/d_{50} = 31$ and 21.

3.2 Deformation in granular materials

Figure 15 illustrates the deformation responses of the granular beds when z_P reached 150 mm. Focusing on the deformation patterns of the layer, for $B/d_{50} \geq 31$, we observed that large deformation was localized as indicated by the arrow in the enlarged views of Fig. 15a, b. For $B/d_{50} < 31$, although bed deformation occurred, localized deformation could not be clearly observed (see online resource 1). The results demonstrated that changes in the granular behaviors as well as penetration resistance occurred between $B/d_{50} = 31$ and 21. According to the above results, we develop discussions mainly based on the comparisons between the large B/d_{50} case (Case A: $B/d_{50} = 63$) and small B/d_{50} case (Case C: $B/d_{50} = 21$) hereafter.

To observe the deformation in more detail, we investigated the bed dilatancy characteristics. Tapia et al. [2] experimentally demonstrated that the bulk volume increased with the penetration depth in densely packed beds. Using DEM simulation, the local compaction and dilation in beds could easily be evaluated. The local packing fraction φ_{local} distributions were obtained by calculating the total particle volume inside a spherical sampling volume with a radius of $R_c = 4d_{50}$ located at the center of each particle. Figure 16a, b illustrate the results of Case A ($B/d_{50} = 63$) and Case C ($B/d_{50} = 21$) corresponding to Fig. 15a, c, respectively. For $B/d_{50} = 63$, narrow dilated regions with a low φ_{local} ($\approx$ 0.57–0.60) emerged diagonally from the plate tip to the free surface. It is clearly confirmable that the narrow dilated regions correspond to the large deformation regions indicated in Fig. 16a. Moreover, φ_{local} remained unchanged and a dense packing

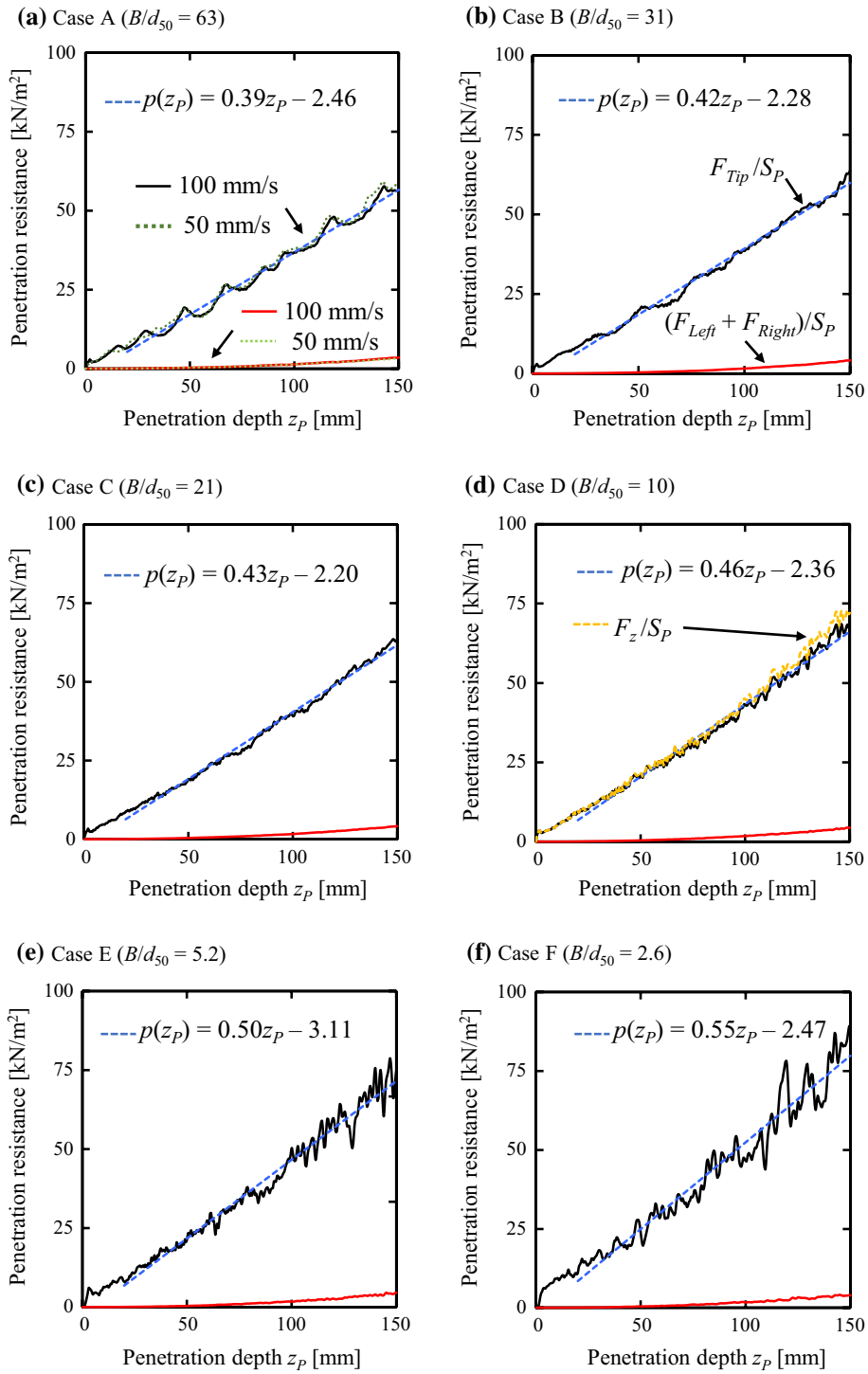

Fig. 10 Penetration resistance acting on the plate as function of penetration depth z_P. Front surface F_{Tip} (black solid lines), and the sum of tangential forces on the left surface F_{Left} and right surface F_{Right} (red solid lines). Linear fitting lines $p(z_P)$ for F_{Tip}/S_P (dashed lines) in the depth $z_P \geq 20$ mm. In **a**, the green dotted lines show the resistances for the slow penetration case $V_P = 50$ mm/s, the yellow dashed line in **d** shows the total resistance F_z/S_P (color figure online)

state was maintained in the other regions. From the results of the numerical simulations of plate drag in dense dry glass beads, Kobayakawa et al. [43] demonstrated that the low φ_{local} was localized near the shear bands, and the values were approximately 0.580–0.590. For $B/d_{50} = 21$, the dilated regions with a low φ_{local} ($\approx$ 0.57–0.60) could be observed only in front of the plate tip. It appears that the slightly dilated regions were widely distributed from the plate tip to the free surface (see online resource 2).

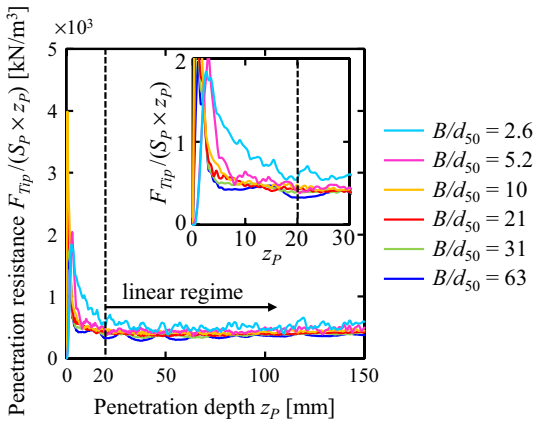

Fig. 11 Transitions of F_{Tip} with respect to penetration depth using $F_{Tip}/(S_P \times z_P)$. The inset shows a magnified view of the transition depth ($z_P \sim 20$ mm) from the initial regime to the linear regime

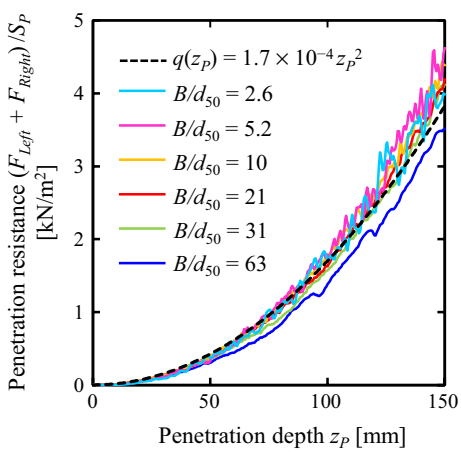

Fig. 12 B/d_{50} dependence of the lateral penetration resistance. The curve $q(z_P)$ (black dashed line) is a quadratic regression fit to the all the cases

3.3 Granular flows

The contours in Fig. 17 indicate the magnitudes of the individual particle velocity $|\boldsymbol{v}_i|$ normalized by the plate penetration speed V_P in the vertical cross-section for Case A ($B/d_{50} = 63$) and Case C ($B/d_{50} = 21$) when the tip resistance F_{Tip} was in the linear regime in $z_P = 47$–67 mm. Moreover, the directions of the mean velocity fields $\boldsymbol{u}$ at $z_P = 57$ are plotted in Fig. 17c, h, where the vectors have the same length regardless of their magnitude. For all cases, the granular flows were confined to a region formed from below the plate tip up to the free surface. The materials outside this region were undisturbed and almost at rest. The boundaries between the disturbed flow region and undisturbed region (dashed lines in Fig. 17c, h) resemble the outlines (arcs *a–d* and *a–e*) of the failure surfaces introduced in the theory of Meyerhof [24], as indicated in Fig. 18. Focusing on the flow region, for all cases, we observed a wedge-shaped flow formed in front of the plate tip, moving with approximately plate speed ($|\boldsymbol{v}_i|/V_P \approx 1$). It is observable that the size of the wedge-shaped flow region varies in the z direction as the plate penetration proceeds for the $B/d_{50} = 63$ case, while it remains approximately constant for $B/d_{50} = 21$ (see online resource 3). This characteristic flow below the plate tip was called the *dead zone* or *stagnant zone* in Murthy et al. [5], Viswanathan et al. [6], Kang et al. [7], Feng et al. [12], and Aguilar et al. [30]. In plastic failure theories [22–25], it is assumed that an elastic wedge zone in front of the plate behaves as part of the plate. As illustrated in Fig. 18, in the case of cohesionless granular materials, the resistance force working on the plate tip is balanced with the sum of the vertical component of the plunging force working on the wedge and the wedge weight. Hence, the wedge size is an important factor to consider for the resistance. In these theories, it is assumed that the wedge width in the y direction is the same as the plate thickness, and the wedge height in the z direction

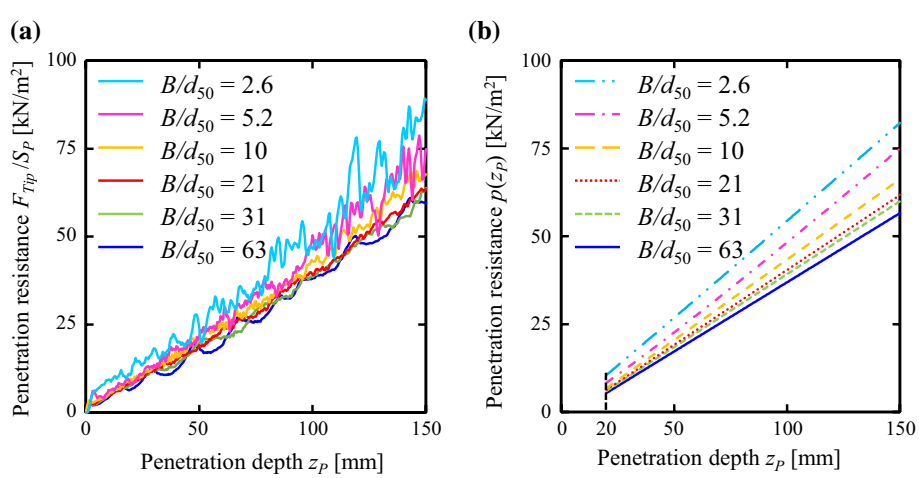

Fig. 13 B/d_{50} dependence of the penetration resistance, showing **a** raw data F_{Tip}/S_P and **b** fitting lines $p(z_P)$

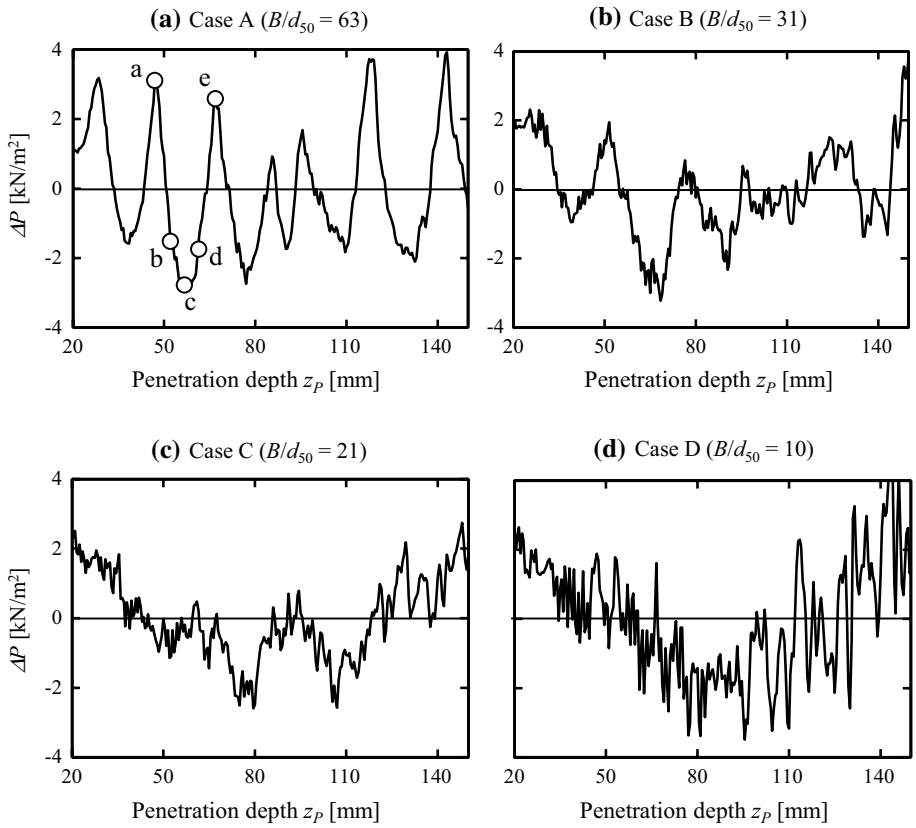

Fig. 14 Fluctuations of tip resistance $\Delta P = F_{Tip}/S_P - p(z_P)$. **a** $B/d_{50} = 63$, **b** $B/d_{50} = 31$, **c** $B/d_{50} = 21$, and **d** $B/d_{50} = 10$

is determined from the internal frictional angle of the granular material and plate roughness, regardless of the particle size. Moreover, because the theories were constructed under static equilibrium conditions, the wedge zone dynamics during the penetration process have not been considered at all. Kang et al. [7] and Feng et al. [12] have proposed a model considering the dynamics of the wedge zone. Feng et al. explained that the initial rapid increase of resistance was caused by an initial compression of the material immediately ahead of the intruder. The transition from the nonlinear to the linear regime was due to the growth of a wedge zone in the penetration direction, and the resistance increased linearly after the wedge zone reached a steady size. As shown in Fig. 17, on the contrary, our results showed that for the $B/d_{50} = 63$ case, the wedge shape did not keep a steady-state even after the tip resistance had already reached the linear regime ($z_P \geq 20$ mm). Feng et al. conducted their penetrations in loose materials ($\varphi_0 = 0.575$), while we focused on dense materials ($\varphi_0 = 0.63$). In our previous study, we investigated the influence of the initial packing fraction on the plate drag [43], and found that a stable granular flow could be observed in front of the plate for a loose material ($\varphi_0 = 0.586$), whereas an unsteady granular flow was observed for the dense material ($\varphi_0 = 0.638$). It is expected that this qualitative difference in behavior can be attributed to the difference in the initial packing fraction.

To investigate the dynamics of the wedge-shaped flow in the height (z) direction, we plotted the temporal change in the normalized vertical particle velocity u_z/V_P distributions along the vertical centerline of the plate for $B/d_{50} = 63$ and 21 in Fig. 19, where u_z is the vertical component of the mean velocity field $\boldsymbol{u}$. In both cases, firstly, at the initial moment the plate penetrates the material, a flow region with the middle velocity ($u_z/V_P \approx 0.5$) propagates deeply into the material, which induces the initial rapid increase of the tip resistance; secondly, the growth of the flow region corresponding to the wedge zone was observed by the early stage ($z_p < 20$–30 mm). In the linear regime, for $B/d_{50} = 63$, a quasi-periodic change occurred in the flow region and the onset of rapid forward expansions of the flow region could be observed at certain points, such as point a ($z_P = 47$ mm) and point e ($z_P = 67$ mm). In contrast, for $B/d_{50} = 21$, a quasi-periodic change in the flow region was not clearly observed. To examine the flow region in more detail, Fig. 20 presents the u_z/V_P distributions for $B/d_{50} = 63$ and 21 at five different penetration depths corresponding to points a–e and f–j in Fig. 19, respectively. The figure indicates that u_z/V_P was almost in unity with the plate tip, and decreased with an increasing distance from the plate tip. To investigate the expansion processes of $B/d_{50} = 63$ (Fig. 20a), the u_z/V_P distributions at point a ($z_P = 47$ mm) and point b ($z_P = 52$ mm) are compared. Particles existing at a 70 mm distance from

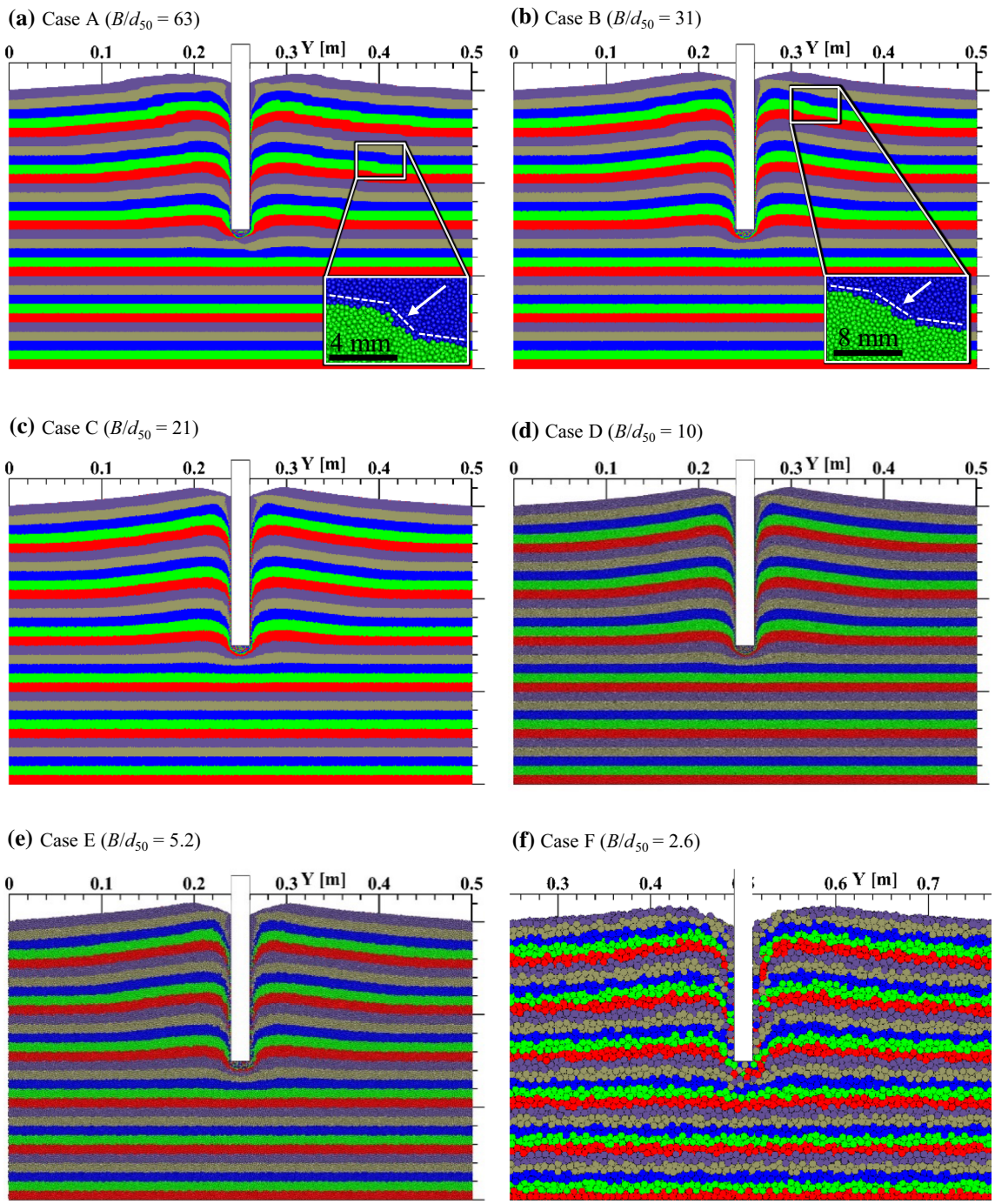

Fig. 15 Deformation of beds at penetration depth $z_P = 150$ mm. The animation of these figures is shown in online resource 1. Insets in **a** and **b** display magnified views of localized large deformations

the free surface exhibited forward velocity when the plate tip reached point a, while they were almost at rest at point b. At the onset of the flow expansions (point a), the flow region was instantaneously propagated far forward from the plate tip. Focusing on the length of the flow region with a high velocity ($u_z/V_P > 0.95$), it increased to 9 mm from the plate tip at point b, compared to 3 mm at point a. This indicates that a finite time scale exists for the development of a high-velocity flow region in front of the plate tip. At point e ($z_P = 67$ mm), similarly to point a, instantaneous propagation of the low-velocity flow region occurred again, while expansion of the high-velocity flow region still did not occur. These results reveal that the flow regions were not in a steady state at all; moreover, deeper rapid expansions of

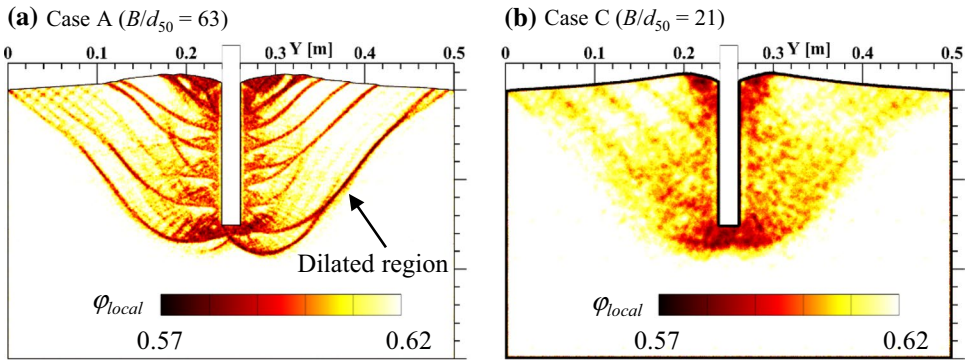

Fig. 16 Distributions of local packing fraction φ_{local} in beds at $z_P = 150$ mm. The animation of these figures is shown in online resource 2

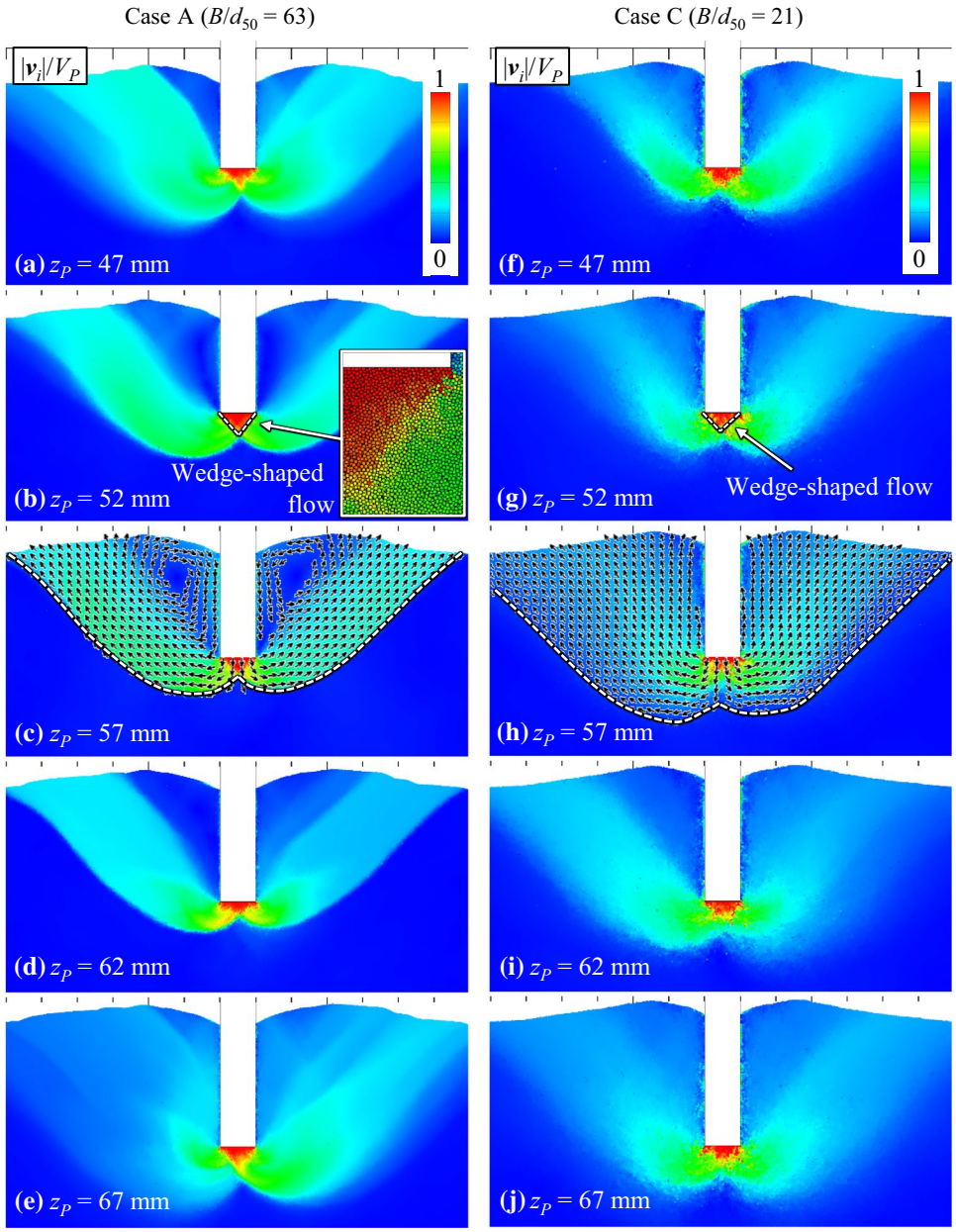

Fig. 17 Distributions of individual particle velocities $|\boldsymbol{v}_i|/V_P$ from $z_P = 47$–67 mm for **a**–**e** $B/d_{50} = 63$ and **f**–**j** $B/d_{50} = 21$. The animation of these figures is shown in online resource 3. In **c** and **h**, the direction of the mean velocity vector $\boldsymbol{u}$ is illustrated when $|\boldsymbol{u}| \geq 0.9$

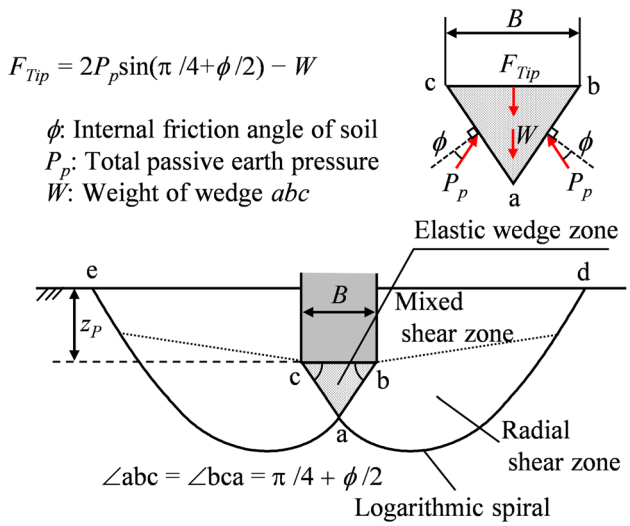

Fig. 18 For cohesionless granular materials, resistance force working on the plate tip predicted by Meyerhof's theory [24]

the flow region occurred first, with the high-velocity flow region subsequently formed near the plate tip, and these processes were repeated (see online resource 3). In contrast, for $B/d_{50}=21$ (Fig. 20b), the u_z/V_P distributions in the flow region remained almost unchanged along with the plate movement. A jump in the height of the high-velocity flow region could not be confirmed.

Figure 21 illustrates the temporal changes in the normalized velocity u_z/V_P distributions in the width (y) direction at the position of one mean particle radius ahead of the plate tip for $B/d_{50}=63$ (Case A), 5.2 (Case E), and 2.6 (Case F). The horizontal axis represents the distance from the plate center. It can be observed that the fast downward flow regions were confined beneath the plate. For each B/d_{50} case, the width of the flow region remained approximately constant and independent of the penetration depth. Meanwhile, it is clearly observable that the width of the flow region changed corresponding to the particle size d_{50}. This result indicates that the wedge width has a dependence on the particle size as well as plate width. We assumed that the wedge width was related to the size of the region in which particles can make direct contact with the plate tip. As illustrated in Fig. 22, this direct contact region is wider, by one particle diameter, than the path of the plate. Here, we introduced an effective plate thickness of $B_{Eff}=B+d_{50}$. The concept is similar to the effective penetration depth and effective vane diameter proposed by Soller and Koehler [44]. They performed experiments with rotating vanes in glass beads and investigated the influence of the vane and bead diameters. They demonstrated that the measured rotational drag and lift forces working on the vane increased with the bead size, and followed a scaling behavior that depended on the effective penetration

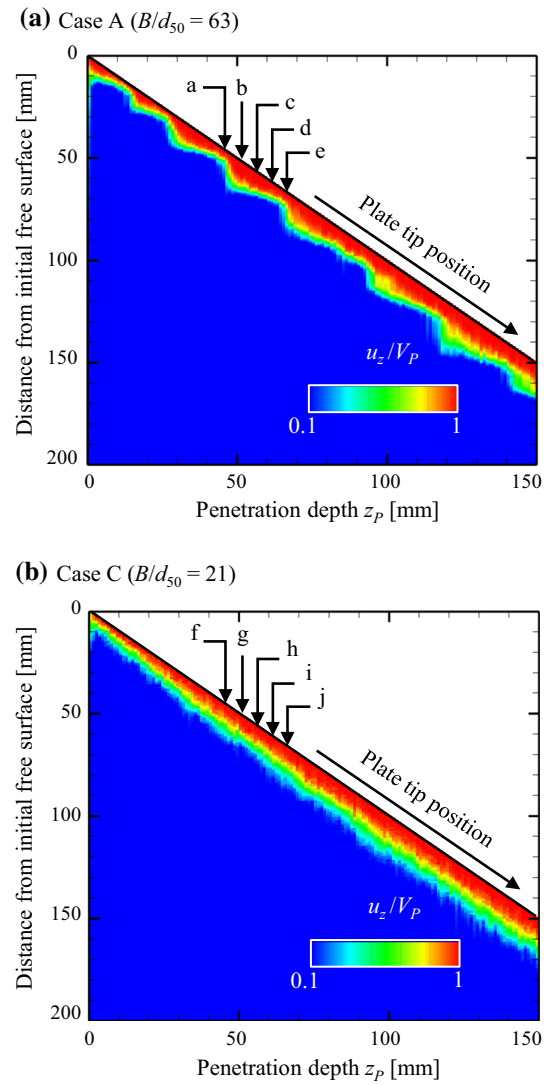

Fig. 19 Change in normalized vertical velocity u_z/V_P distributions along center of plate in penetration (z) direction

depth and effective vane diameter, expressed as a function including particle size. Figure 23 illustrates the tip penetration resistance F_{Tip}/S_{Eff}, where S_{Eff} is defined by $S_{Eff}=(B+d_{50})\times D$. It was found that the mean tip penetration resistances using the effective plate thickness almost agreed with one another. This result indicates that, as the particle size became larger, the effective plate thickness increased and, as a result, the mean tip penetration resistance increased with the particle size.

3.4 Shear band

Localizations of large deformations, known as shear bands, are induced by intruders in granular beds. Vesic [25] experimentally demonstrated that for a densely packed bed, shear band formation emerges from the edges of an intruder tip

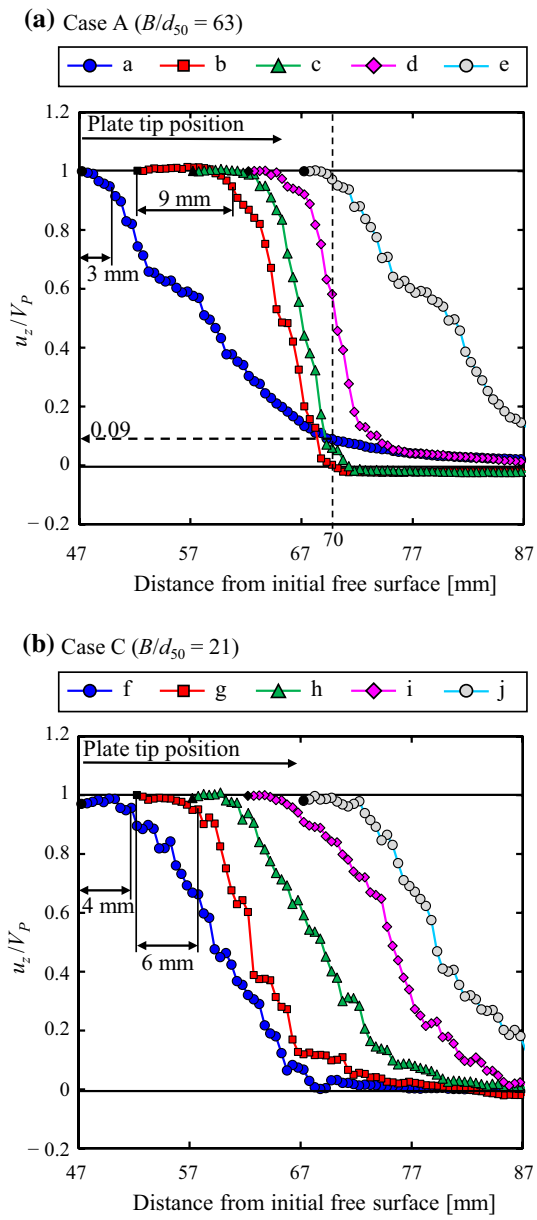

Fig. 20 u_z/V_P at the five different penetration depth which correspond to points a–j in Fig. 19

and extends downwards and laterally outwards in the shallow penetration regime. The propagation of shear bands has been observed by the particle-tracking technique [5] and numerical particle simulation [6]. To identify the shear bands in the granular materials, the shear strain rate in the beds was computed. It was demonstrated that each shear band firstly started from the edges of an intruder tip, and the bands propagated downwards and intersected below the plate tip. It could be observed that two shear bands formed a wedge zone below the plate tip. These authors only focused on very shallow penetration depths ($z_P < B$) and did not discuss the behaviors of shear bands after they were formed in detail. Hamm et al. [1] and Tapia et al. [2] experimentally demonstrated that shear bands are nucleated and disappear repeatedly as the penetration depth increases further. Moreover, they reported that the evolution of shear bands is largely dependent on the initial bulk packing fraction. Because they were not using plates with a flat-tip, they did not report on the existence of a wedge zone.

To identify the shear band in the materials, we computed the maximal shear strain rate $\dot{\gamma}$ from the DEM results by

$$\dot{\gamma} = \sqrt{\left(\frac{\dot{e}_{yy} - \dot{e}_{zz}}{2}\right)^2 + \dot{e}_{yz}^2}, \tag{9}$$

where $\dot{e}_{yy}$ and $\dot{e}_{zz}$ are the normal strain rates, and $\dot{e}_{yz}$ is the shear strain rate, given by

$$\dot{e}_{yy} = \frac{\partial u_y}{\partial y}, \tag{10}$$

$$\dot{e}_{zz} = \frac{\partial u_z}{\partial z}, \tag{11}$$

$$\dot{e}_{yz} = \frac{1}{2}\left(\frac{\partial u_y}{\partial z} + \frac{\partial u_z}{\partial y}\right). \tag{12}$$

Figure 24 illustrates the maximal shear strain rate fields for Case A ($B/d_{50} = 63$) and Case C ($B/d_{50} = 21$). These snapshots correspond to the distributions of particle velocities in Fig. 17. In both cases, it can be observed that the shear bands in front of the tip bordered a wedge-shaped region (ΔABC in Fig. 24c, h), corresponding to the flow region with a high velocity. For large B/d_{50} cases, it can clearly be observed that the shear bands were developed from the plate edges to the free surface; in contrast, this is not as clear for small B/d_{50} cases (see online resource 4). These results are consistent with those of our previous study [31]. In the present study, we investigated the B/d_{50} dependence on the dynamics of the shear band formation in further detail. To develop further discussions, the shear bands are distinguished as (I) and (II), as indicated in Fig. 24c, h. Shear bands (I) are indicated by solid lines, and these were developed respectively from the plate edges B and C to intersection point A, and were bordering a wedge zone (ΔABC). Shear bands (II) are indicated by dashed lines, and developed from near intersection point A to the free surface (points D and E).

Shear bands (I) In the theories based on static equilibrium, the wedge zone is assumed to be a triangle with angles $\pi/2 + \phi/2$, and it does not change according to time. In contrast, for $B/d_{50} = 63$, the simulation results demonstrate that the wedge angles changed during the penetration. Figure 25a illustrates the temporal change in the angles of shear bands (I) ψ_R and ψ_L, and the resistance fluctuation ΔP for Case A

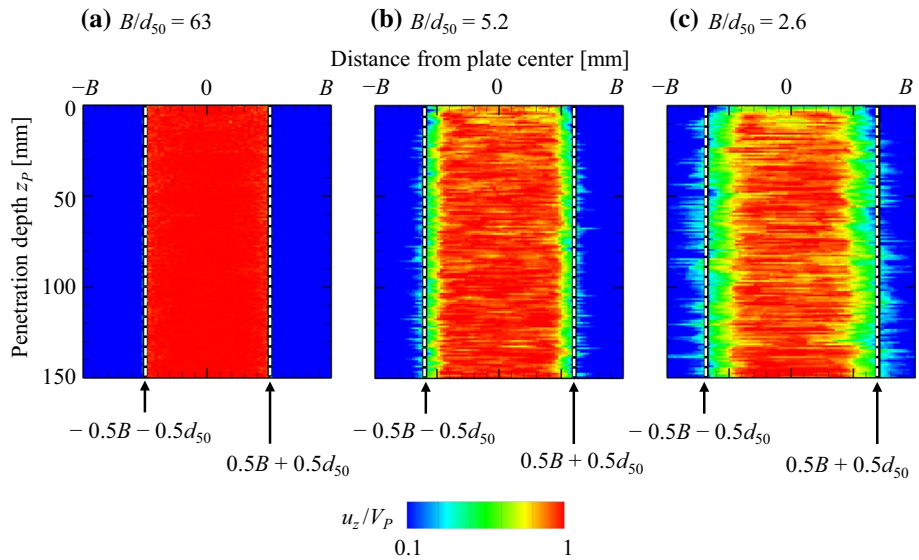

Fig. 21 Change of the normalized vertical velocity u_z/V_P distributions in the width (y) direction at the position one particle radius ahead of the plate tip

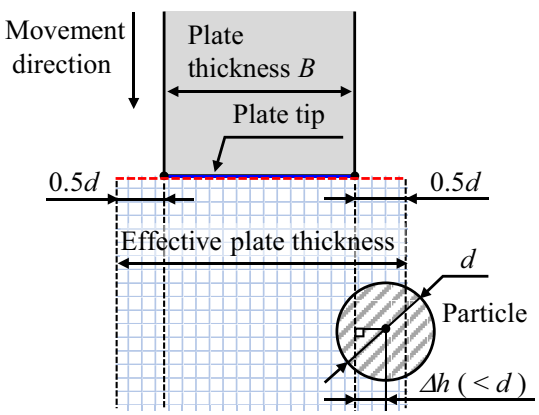

Fig. 22 Effective plate thickness $B_{Eff} = B + d_{50}$

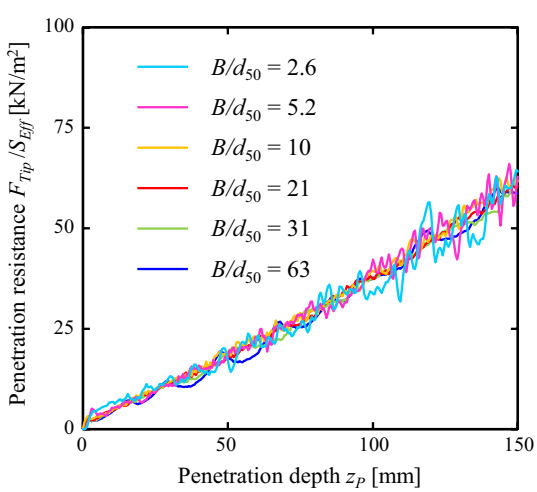

Fig. 23 Tip penetration resistance using effective plate width as function of penetration depth z_P

($B/d_{50} = 63$), where ψ_R and ψ_L indicate the angles ∠ABC and ∠BCA in Fig. 24c, respectively. From the figure, we found that for $B/d_{50} = 63$, ψ_R and ψ_L exhibited quasi-periodic fluctuations, and sudden jumps from between 51° and 71° to between 19° to 41° occurred on both sides. At the timing of the jump events, new shear bands were formed (solid lines in inset of Fig. 24e), while the former shear bands (dotted lines in inset of Fig. 24e) could still be observed. It is noted that the angle of the new shear bands is plotted in Fig. 25 for the case where former and new bands could be observed simultaneously. Figure 25 illustrates that the onset of new band formation sometimes occurred synchronously on both sides. A short while after the new band was formed, the former bands disappeared. The resistance force reached the local maximum when the former bands disappeared. However, for $B/d_{50} = 21$, the magnitude of the fluctuations in ψ_R and ψ_L was smaller (34°–67°), and no clear periodicity was exhibited (Fig. 25b). According to Figs. 24f–j and 25b, it appears that the bands continued to form in front of the tip without disappearance, and there was no clear correlation between the angles and resistance. For both cases, the mean values of the angles gradually increased with the penetration depth. The mean angles between $z_P = 110$ and 150 mm were 55° for both cases. *Shear bands (II)* Shear bands (II) could be observed clearly for $B/d_{50} = 63$, but not for $B/d_{50} = 21$. For $B/d_{50} = 63$, the evolution of bands (II) was related to the evolution of bands (I). At the timing of the inception of bands (I), several new bands (II) emerged from near intersection point A (dashed-dotted lines in Fig. 24e). Thereafter, it appears that these newly formed bands (II) could not sustain themselves, and only one band with large shear strain remained on each side as a result (Fig. 24b–d). In contrast, for $B/d_{50} = 21$, it appears that the inception and disappearance of new shear bands (II) were repeated frequently during

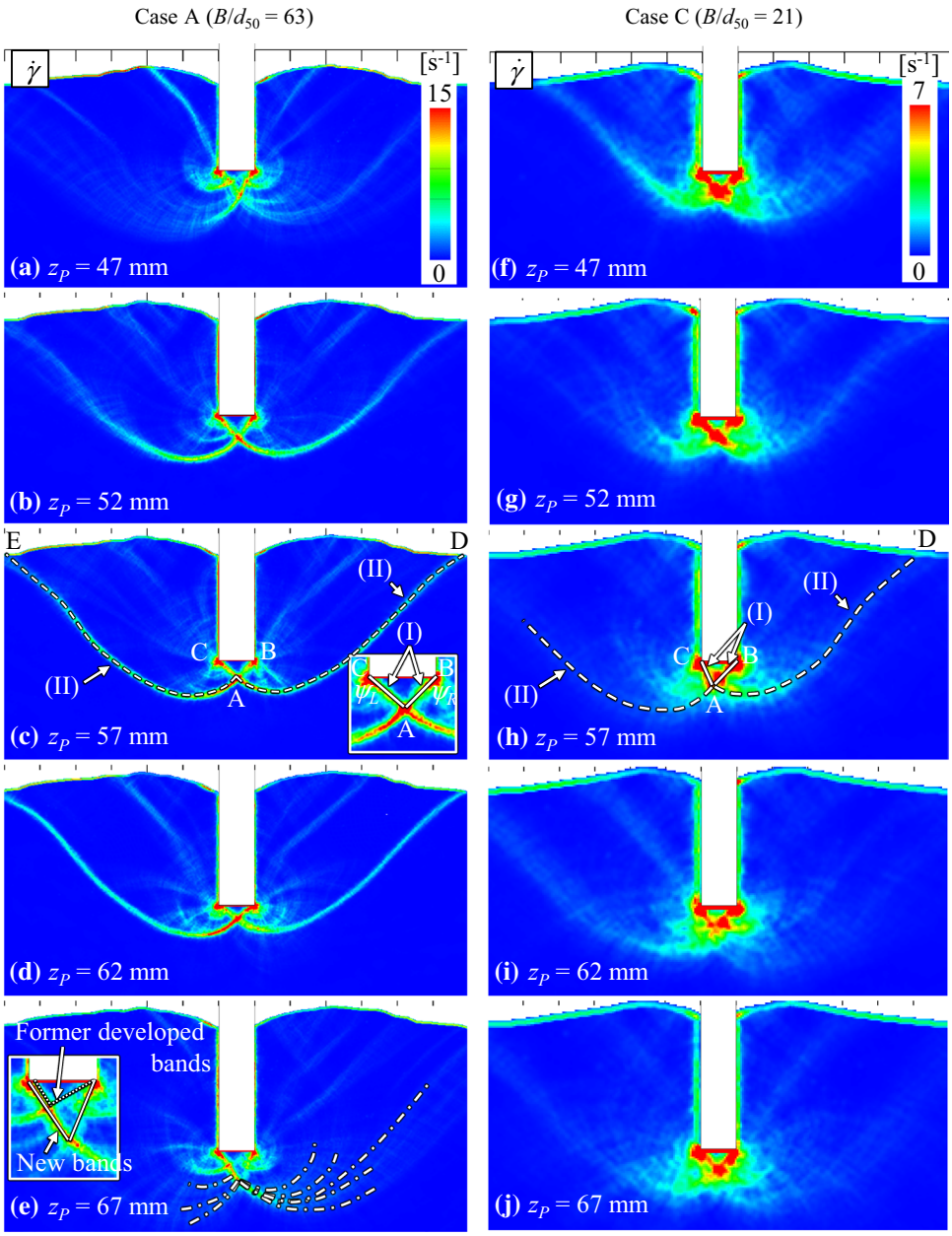

Fig. 24 Shear strain rate fields from z_P = 47–67 mm for **a**–**e** B/d_{50} = 63 and **f**–**j** B/d_{50} = 21. The animation of these figures is shown in online resource 4. As shown in **c** B/d_{50} = 63 and **h** B/d_{50} = 21 at z_P = 57 mm, shear band (I) formed from plate edges B and C to intersection point A (indicated by solid lines), and shear band (II) formed from near intersection point A to the free surface (points D and E). In the inset of **c**, ψ_R and ψ_L indicate the angles of shear bands (I) ∠ABC and ∠BCA

the penetration, and clear local concentration of shear strains was not observed.

To investigate the mechanism of the B/d_{50} dependence on the shear band formation, we focused on the relationship between the shear band formation and microscopic particle motion. It has been reported that the rotations of individual particles become significant inside shear bands [45–47]. Figure 26 illustrates the magnitude of the normalized angular velocity of the individual particle $\bar{\omega}_i$ for Case A (B/d_{50} = 63) and Case C (B/d_{50} = 21), where $\bar{\omega}_i$ is defined by

$$\bar{\omega}_i = \frac{d_p|\boldsymbol{\omega}_i|}{2V_P}. \tag{13}$$

In the case where there is no slip between a particle and a plate moving toward the direction parallel to the plate surface, the particle rotation induced by the contact is given by $\bar{\omega}_i = 1$. These snapshots represent the results at z_P = 57 mm and corresponding to Fig. 24c, h. A clear correlation is confirmed between the high shear region (Fig. 24c, h) and high angular velocity region (Fig. 26), as expected. Figure 27 illustrates the $\bar{\omega}_i$ distributions along the dashed lines passing through plate edge C in Fig. 26. The solid lines represent the values averaged over each maximum particle diameter interval. For B/d_{50} = 63, $\bar{\omega}_i$ near the plate tip and at a distance of approximately 17 mm from the tip were clearly higher, corresponding to shear bands (I) and (II), respectively. Following Bardet and Proubet [46], we estimated the

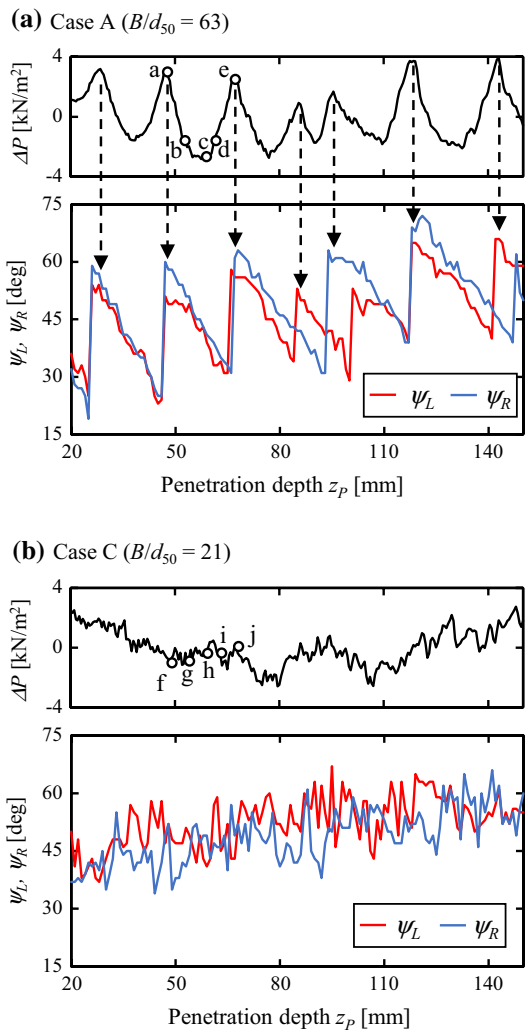

Fig. 25 Dynamics of the wedge region below the plate tip for **a** $B/d_{50}=63$ and **b** $B/d_{50}=21$

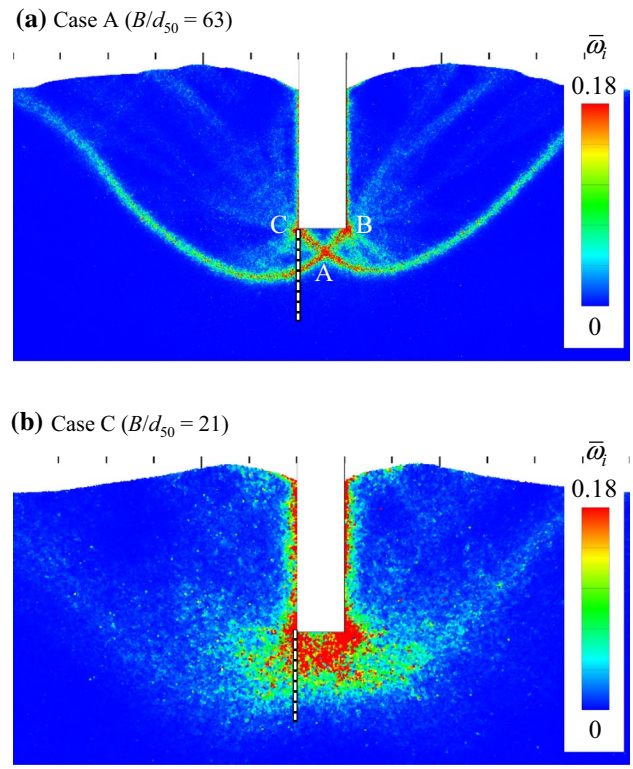

Fig. 26 Distribution of normalized angular velocity of particles at $z_P=57$ mm for **a** $B/d_{50}=63$ and **b** $B/d_{50}=21$. Figure 27 shows the normalized angular velocity distributions along the dashed lines passing through plate edge C

shear band thickness by measuring the distance between two points on the line crossing band (II), at which the magnitude of the particle rotation became sufficiently small. At $z_P=57$ mm, the distance along the dashed line was $21d_{50}$ (6.8 mm). Because the angle between the dashed line and band was approximated as 64°, the shear band thickness was estimated as $19d_{50}$. For $B/d_{50}=21$, $\bar{\omega}_i$ near the plate tip was large, and decreased as the distance from the plate tip increased. We could not confirm a local peak corresponding to shear band (II). Various researchers [32, 48–52] have reported that the shear band thickness is strongly affected by the absolute size of the particles. Nemat-Nasser and Okada [50] reported that when the mean particle diameters d_{50} were

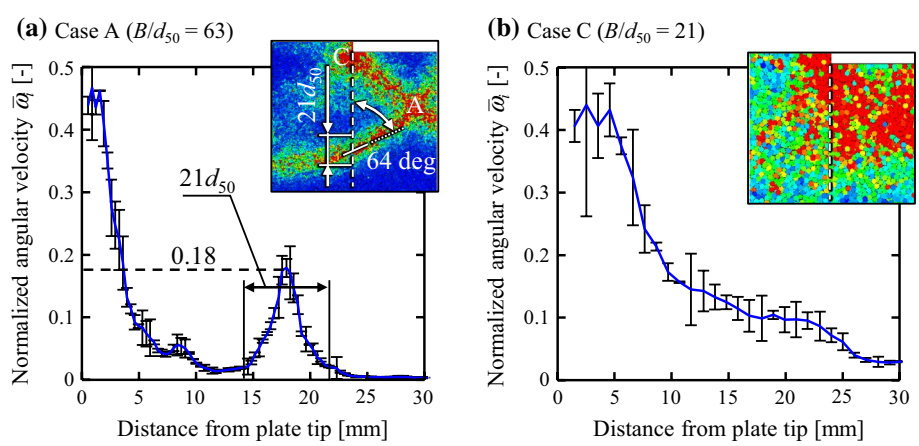

Fig. 27 Angular velocity distribution along left plane of the plate for **a** $B/d_{50}=63$ and **b** $B/d_{50}=21$. Error bars indicate the standard deviations within each sampling space

0.22 and 0.48 mm, the band thicknesses were $11d_{50}$ and $15d_{50}$, respectively. Viggiani et al. [51] also reported that, for $d_{50}=0.34$ and 0.90 mm, the band thicknesses were between $10d_{50}$ and $15d_{50}$ and $8d_{50}$, respectively. These results indicate that the ratio of the band thickness to the mean particle diameter was almost constant, even though the particle size changed. In contrast, Vangla and Latha [52] observed that the band thickness decreased from between $21d_{50}$ and $24d_{50}$ to between $10d_{50}$ and $12d_{50}$ when the mean particle size increased from 0.22 to 0.87 mm. Owing to the particle size dependence of the shear band thickness, with a decreasing B/d_{50}, the thickness became relatively larger with respect to the plate thickness. When B/d_{50} became approximately 20 or less, the band thickness became almost the same or larger than the plate width. For all cases, shear bands (I) interfered with shear bands (II), and evolutions of the wedge zone formed by bands (I) and the strain concentration in bands (II) did not occur in any cases.

4 Conclusions

We investigated the influence of particle size on vertical plate penetration into granular materials by large-scale DEM simulations. Particle size d_{50} was varied from 0.32 to 7.68 mm while keeping the plate thickness B to 20 mm for all the cases. Hence, B/d_{50} was varied from 2.6 to 63. For $B/d_{50}=63$, the size ratio reaches almost the same level with laboratory experiments in the literatures [1, 2]. As parameters that give major effects on the penetration resistance, initial packing fraction of the beds was kept high and penetration depth was kept in a shallow regime.

We confirmed that the mean penetration resistance acting on the plate tip surface increases with a decrease of B/d_{50}, which is consistent with the experiments by Bolton et al. [14]. From the observations of granular flow and shear band formation, a wedge-shaped granular flow with high forward velocity was observed in front of the plate tip for all the cases and it was similar to the wedge zone assumed in classical plastic failure theories. Only for the large B/d_{50} cases ($B/d_{50}=63$ and 31), quasi-periodic fluctuations of the resistance similar to those reported by Hamm et al. [1] and Tapia et al. [2] could be observed. We have investigated the influence of particle size effect on the processes of granular flow and shear band propagation at the particle-scale and the following findings were revealed:

1. The width of wedged-flow formed in front of the plate tip was larger than the plate thickness almost by a mean particle diameter. The effective plate thickness increased as the particle size became larger and the mean tip resistance increased with particle size as a result. Moreover, the tangential force acting on the side surfaces does not change with B/d_{50}.
2. Tip resistance increases linearly with penetration depth, while the tangential resistances increase with the depth squared, regardless of B/d_{50}.
3. The behavior of tip resistance fluctuations changes depending on B/d_{50}. In particular, the behavior changed qualitatively between $B/d_{50}=31$ and 21. For the large B/d_{50} cases, tip resistance fluctuations became quasi-periodic; conversely, for the small B/d_{50} cases, the fluctuations did not show a clear periodicity.
4. For the large B/d_{50} case, the shear bands nucleated and disappeared quasi-periodically during penetrations. The tip resistance fluctuations were attributed to the band evolutions. Due to particle size dependence of shear band thickness, as decreasing B/d_{50}, the thickness is relatively larger with respect to the plate thickness. When B/d_{50} becomes about 20 or less, the band thickness is almost same or larger than the plate thickness. As a result, for the small B/d_{50} case, the evolutions of the bands formed the wedge zone could not be observed. The periodic resistance fluctuations did not occur.
5. The behavior of wedged-flow in the vertical direction changes depending on B/d_{50}. For the large B/d_{50} case, the height of the wedged-flow oscillated quasi-periodically. The evolutions of the wedged-flow in the vertical direction were corresponded to the evolutions of shear bands. For the small B/d_{50} case, neither the wedged-flow evolutions nor evolutions of shear bands occur.

This study shows that for plate penetration into dense cohesionless granular materials in a shallow penetration regime, the value of B/d_{50} affects not only the penetration resistance but also granular flow and shear band formation in the beds. We recommend that B/d_{50} should be more than 30 to neglect particle size effect.

Acknowledgements All computations were performed using Subsystem A in Research Institute for Information Technology, Kyushu University.

Compliance with ethical standards

Conflict of interest Shinichiro Miyai has an employment relationship with Komatsu Ltd. Shinichiro Miyai and Murino Kobayakawa are researchers of Komatsu MIRAI construction equipment cooperative research center in Osaka University funded by Komatsu Ltd. Takuya Tsuji and Toshitsugu Tanaka are professors (concurrent) in Komatsu MIRAI construction equipment cooperative research center.

Open Access This article is distributed under the terms of the Creative Commons Attribution 4.0 International License (http://creativecommons.org/licenses/by/4.0/), which permits unrestricted use,

distribution, and reproduction in any medium, provided you give appropriate credit to the original author(s) and the source, provide a link to the Creative Commons license, and indicate if changes were made.

References

1. Hamm, E., Tapia, F., Melo, F.: Dynamics of shear bands in a dense granular material forced by a slowly moving rigid body. Phys. Rev. E **84**(4), 041304 (2011)
2. Tapia, F., Espindola, D., Hamm, E., Melo, F.: Effect of packing fraction on shear band formation in a granular material forced by a penetrometer. Phys. Rev. E **87**(1), 014201 (2013)
3. Peng, Z., Xu, X., Lu, K., Hou, M.: Depth dependence of vertical plunging force in granular medium. Phys. Rev. E **80**(2), 021301 (2009)
4. Brzinski III, T.A., Mayor, P., Durian, D.J.: Depth-dependent resistance of granular media to vertical penetration. Phys. Rev. Lett. **111**(16), 168002 (2013)
5. Murthy, T.G., Gnanamanickam, E., Chandrasekar, S.: Deformation field in indentation of a granular ensemble. Phys. Rev. E **85**(6), 061306 (2012)
6. Viswanathan, K., Mahato, A., Murthy, T.G., Koziara, T., Chandrasekar, S.: Kinematic flow patterns in slow deformation of a dense granular material. Granul. Matter **17**(5), 553–565 (2015)
7. Kang, W., Feng, Y., Liu, C., Blumenfeld, R.: Archimedes' law explains penetration of solids into granular media. Nat. Commun. **9**(1), 1101 (2018)
8. Stone, M., Barry, R., Bernstein, D., Pelc, M., Tsui, Y., Schiffer, P.: Local jamming via penetration of a granular medium. Phys. Rev. E **70**(4), 041301 (2004)
9. Nazhat, Y., Airey, D.: The kinematics of granular soils subjected to rapid impact loading. Granul. Matter **17**(1), 1–20 (2015)
10. Tordesillas, A., Steer, C.A.H., Walker, D.M.: Force chain and contact cycle evolution in a dense granular material under shallow penetration. Nonlinear Process. Geophys. **21**(2), 505–519 (2014)
11. Kolb, E., Cixous, P., Charmet, J.: Flow fields around an intruder immersed in a 2D dense granular layer. Granul. Matter **16**(2), 223–233 (2014)
12. Feng, Y., Blumenfeld, R., Liu, C.: Support of modified Archimedes' law theory in granular media. Soft Matter **15**(14), 3008–3017 (2019)
13. Jiang, M., Zhu, H., Harris, D.: Classical and non-classical kinematic fields of two-dimensional penetration tests on granular ground by discrete element method analyses. Granul. Matter **10**(6), 439–455 (2008)
14. Bolton, M.D., Gui, M.W., Garnier, J., Corte, J.F., Bagge, G., Laue, J., Renzi, R.: Centrifuge cone penetration tests in sand. Geotechnique **49**(4), 543–552 (1999)
15. Kobayashi, T., Fukagawa, R.: Characterization of deformation process of CPT using X-ray TV imaging technique. In: Benedetto, D. et al. (eds.) Proceedings of the 3rd International Symposium on Deformation Characteristics of Geomaterials, pp. 43–47 (2003)
16. Butlanska, J., Arroyo, M., Gens, A.: Size effects on a virtual calibration chamber. In: Benz, T., Nordal, S. (eds.) Proceedings of the 7th European Conference on Numerical Methods in Geotechnical Engineering, pp. 225–230 (2010)
17. Arroyo, M., Butlanska, J., Gens, A., Calvetti, F., Jamiolkowski, M.: Cone penetration tests in a virtual calibration chamber. Geotechnique **61**(6), 525–531 (2011)
18. Tran, Q.A., Chevalier, B., Breul, P.: Discrete modeling of penetration tests in constant velocity and impact conditions. Comput. Geotech. **71**, 12–18 (2016)
19. Falagush, O., McDowell, G.R., Yu, H.S., de Bono, J.P.: Discrete element modelling and cavity expansion analysis of cone penetration testing. Granul. Matter **17**(4), 483–495 (2015)
20. Lin, J., Wu, W.: Numerical study of miniature penetrometer in granular material by discrete element method. Philos. Mag. **92**(28–30), 3474–3482 (2012)
21. Liu, S., Wang, J.: Depth-independent cone penetration mechanism by a discrete element method (DEM)-based stress normalization approach. Can. Geotech. J. **53**(5), 871–883 (2015)
22. Prandtl, L.: Concerning the hardness of plastic bodies. Nachr. Ges. Wiss. Gottingen, 74–85 (1920)
23. Terzaghi, K.: Theoretical Soil Mechanics. Chapman and Hall, Limited, London (1951)
24. Meyerhof, G.: The ultimate bearing capacity of foundations. Geotechnique **2**(4), 301–332 (1951)
25. Vesic, A.B.: Bearing capacity of deep foundations in sand. Highw. Res. Rec. **39**, 112–153 (1963)
26. Zhang, Z., Wang, Y.H.: Three-dimensional DEM simulations of monotonic jacking in sand. Granul. Matter **17**(3), 359–376 (2015)
27. Lobo-Guerrero, S., Vallejo, L.E.: Influence of pile shape and pile interaction on the crushable behavior of granular materials around driven piles: DEM analyses. Granul. Matter **9**(3–4), 241–250 (2007)
28. McDowell, G., Bolton, M.: Effect of particle size distribution on pile tip resistance in calcareous sand in the geotechnical centrifuge. Granul. Matter **2**(4), 179–187 (2000)
29. Maciejewski, J., Jarzebowski, A., Trampczynski, W.: Study on the efficiency of the digging process using the model of excavator bucket. J. Terramech. **40**(4), 221–233 (2003)
30. Aguilar, J., Goldman, D.I.: Robophysical study of jumping dynamics on granular media. Nat. Phys. **12**(3), 278–283 (2016)
31. Miyai, S., Kobayakawa, M., Tsuji, T., Sato, M., Imamura, K., Tanaka, T.: DEM study on vertical plate penetration into dry granular materials: influence of particle size. In: Proceedings of the 10th Asia-Pacific Conference on International Society Terrain-Vehicle Systems (2018)
32. Cerato, A.B., Lutenegger, A.J.: Specimen size and scale effects of direct shear box tests of sands. Geotech. Test. J. **29**(6), 507–516 (2006)
33. Miyai, S., Imamura, K.: Analysis of the Interaction Between Soil and the Earth-Moving Equipment. HPCI user report, project ID: hp150310 (2016) **(in Japanese)**
34. Cundall, P.A., Strack, O.D.: A discrete numerical model for granular assemblies. Geotechnique **29**(1), 47–65 (1979)
35. Iwashita, K., Oda, M.: Rolling resistance at contacts in simulation of shear band development by DEM. J. Eng. Mech. **124**(3), 285–292 (1998)
36. Belheine, N., Plassiard, J.P., Donze, F.V., Darve, F., Seridi, A.: Numerical simulation of drained triaxial test using 3D discrete element modeling. Comput. Geotech. **36**(1–2), 320–331 (2009)
37. Ai, J., Chen, J.F., Rotter, J.M., Ooi, J.Y.: Assessment of rolling resistance models in discrete element simulations. Powder Technol. **206**(3), 269–282 (2011)
38. Jiang, M., Shen, Z., Wang, J.: A novel three-dimensional contact model for granulates incorporating rolling and twisting resistances. Comput. Geotech. **65**, 147–163 (2015)
39. Feng, Y.T., Han, K., Owen, D.R.J., Loughran, J.: On upscaling of discrete element models: similarity principles. Eng. Comput. **26**(6), 599–609 (2009)
40. Feng, Y.T., Owen, D.R.J.: Discrete element modelling of large scale particle systems—I: exact scaling laws. Comput. Part. Mech. **1**, 159–168 (2014)
41. Kawaguchi, T., Tanaka, T., Tsuji, Y.: Numerical simulation of two-dimensional fluidized beds using the discrete element method

(comparison between the two-and three-dimensional models). Powder Technol. **96**(2), 129–138 (1998)
42. Tsuji, Y., Kawaguchi, T., Tanaka, T.: Discrete particle simulation of two-dimensional fluidized bed. Powder Technol. **77**(1), 79–87 (1993)
43. Kobayakawa, M., Miyai, S., Tsuji, T., Tanaka, T.: Local dilation and compaction of granular materials induced by plate drag. Phys. Rev. E **98**(5), 052907 (2018)
44. Soller, R., Koehler, S.A.: Drag and lift on rotating vanes in granular beds. Phys. Rev. E **84**, 021305 (2006)
45. Gu, X., Huang, M., Qian, J.: Discrete element modelling of shear band in granular materials. Theor. Appl. Fract. Mech. **72**, 37–49 (2014)
46. Bardet, J.P., Proubet, J.: A numerical investigation of the structure of persistent shear bands in granular media. Geotechnique **41**(4), 599–613 (1991)
47. Oda, M., Konishi, J., Nemat-Nasser, S.: Experimental micromechanical evaluation of strength of granular materials: effects of particle rolling. Mech. Mater. **1**(4), 269–283 (1982)
48. Roscoe, K.H.: The influence of strains in soil mechanics. Geotechnique **20**(2), 129–170 (1970)
49. Scarpelli, G., Wood, D.M.: Experimental observations of shear band patterns in direct shear tests. In: Proceedings of the IUTAM Symposium on Deformation and Failure of Granular Materials, pp. 473–483 (1982)
50. Nemat-Nasser, S., Okada, N.: Radiographic and microscopic observation of shear bands in granular materials. Geotechnique **51**(9), 753–765 (2001)
51. Viggiani, G., Kuntz, M., Desrues, J.: An experimental investigation of the relationships between grain size distribution and shear banding in sand. In: Vermeer, P.A. et al. (eds.) Continuous and Discontinuous Modeling of Cohesive Frictional Materials, Lecture Notes in Physics, vol. 568, pp. 111–127 (2001)
52. Vangla, P., Latha, G.M.: Influence of particle size on the friction and interfacial shear strength of sands of similar morphology. Int. J. Geosynth. Ground Eng. **1**(1), 1–12 (2015)

Publisher's Note Springer Nature remains neutral with regard to jurisdictional claims in published maps and institutional affiliations.